

BIFURCATIONS OF HIGHLY INCLINED NEAR HALO ORBITS USING MOSER REGULARIZATION

CHANKYU JOUNG, DAYUNG KOH, OTTO VAN KOERT

ABSTRACT. We study the bifurcation structure of highly inclined near halo orbits with close approaches to the light primary, in the circular restricted three-body problem (CR3BP). Using a Hamiltonian formulation together with Moser regularization, we develop a numerical framework for the continuation of periodic orbits and the computation of their Floquet multipliers which remains effective near collision. We describe vertical collision orbits and families emerging from its pitchfork, period-doubling, and period-tripling bifurcations in the limiting Hill’s problem, including the halo and butterfly families. We continue these into the CR3BP using a perturbative framework via a symplectic scaling, and construct bifurcation graphs for representative systems (Saturn-Enceladus, Earth-Moon, Copenhagen) to identify common dynamical features. Conley-Zehnder indices are computed to classify the resulting families. Together, these results provide a coherent global picture of polar orbit architecture near the light primary, offering groundwork for future mission design, such as Enceladus plume sampling missions.

1. INTRODUCTION

We study polar orbits, i.e. spatial periodic orbits with large vertical components and close approaches to a primary, in the circular restricted three-body problem (CR3BP). Such orbits are of special interest in space mission design. For instance, the *halo orbit family* is widely used in missions for its advantageous out-of-plane geometry. Nearly rectilinear halo orbits (NRHOs) [HB84] offer repeated close approaches to one celestial body while maintaining continuous visibility of the other, a feature underlying their use in NASA’s planned Lunar Gateway mission [NAS]. NRHOs have also been proposed as science orbits for plume sampling missions to Saturn’s icy moon Enceladus [RL09; Mac+21], which is one of the primary motivations for this study.

We will use a Hamiltonian description of the CR3BP in a uniformly rotating frame,

$$H = \frac{1}{2}|p|^2 + p_1q_2 - p_2q_1 - \frac{1-\mu}{|q - (-\mu, 0, 0)|} - \frac{\mu}{|q - (1-\mu, 0, 0)|}.$$

Here, q and p denote the position and momentum, and $\mu \in [0, 1]$ is the mass ratio of the primaries. We focus on the case μ close to 0 and on motion near the light primary at $q = (1-\mu, 0, 0)$. By rescaling the coordinates and taking the limit $\mu \rightarrow 0$, one obtains the Hill’s problem (see Section 2.3 for details), whose Hamiltonian is

$$H = \frac{1}{2}|p|^2 + p_1q_2 - p_2q_1 - \frac{1}{|q|} + \frac{1}{2}|q|^2 - \frac{3}{2}q_1^2.$$

From an abstract perspective, the limit cases of families of periodic orbits are of particular importance. For example, many periodic orbits in the CR3BP arise as perturbations of periodic orbits in the limiting case of the Hill’s problem, which Hénon referred to as *generating orbits* [Hén97]. In the study of polar orbits, an important example is the *vertical collision orbit* in Hill’s problem, a trajectory confined to the vertical q_3 -axis that reaches a maximum height before ending in a collision, see Figure 4. After regularization, this orbit becomes periodic and serves as an important generating orbit for nearby polar orbits.¹ Recent work by Aydin and Batkhin [AB25] provides a comprehensive study of bifurcating families of multiple covers of the vertical collision orbit within

¹Another limit to consider occurs as the Hamiltonian energy decreases to $-\infty$. After an appropriate rescaling, the dynamics of the energy surface converges to the Kepler problem. In this setting, Moser [Mos70] showed using the averaging method that periodic families bifurcate from a set of four “basic” Keplerian orbits: the retrograde and direct planar circular orbits, and a pair of vertical collision orbits.

Hill’s problem, along with an overview of earlier results [LL83; BB09; BFvK19]. One aim of this work is to reveal how this vertical collision orbit continues into the CR3BP and to organize the bifurcation structure of related families of polar orbits.

A detailed numerical study of near-collision periodic orbits requires a regularization framework compatible with high-precision continuation. The Kustaanheimo-Stiefel (KS) regularization [KS65], as described for the numerical setting in [HB84], has traditionally been used for this purpose. In this study, we adopt an alternative approach based on Moser’s regularization. This framework offers several advantages: it is applicable in arbitrary dimensions (e.g. planar or spatial CR3BP), preserves periodicity of orbits between the regularized and unregularized systems, and provides a direct correspondence of Floquet multipliers (Lemma 3.4), simplifying stability analysis. We provide a first, complete implementation of Moser regularization for numerical continuation and stability analysis of periodic orbits. Our implementation treats the dynamics as a Hamiltonian system with constraints, whose framework we review in Appendix B. In particular, the regularized phase space appears as a 6-dimensional constrained submanifold embedded in an 8-dimensional Euclidean space.

Based on this setup, we investigate the bifurcation structure of polar orbits near the light primary in the Moser regularized CR3BP and in Hill’s problem. We identify the pitchfork, period-doubling, and period-tripling bifurcations of the vertical collision family, the associated branching families, and how these structures persist or change under perturbation from Hill’s problem to the CR3BP. Bifurcation graphs are computed for several representative systems, including the Saturn-Enceladus, Earth-Moon, and Copenhagen problems. A summary of the periodic families and the corresponding results is given in Table 1. Our results provide a global understanding of key orbit families relevant to mission design such as halo and butterfly families, while providing new observations on their behavior near collision. In particular, this work complements and extends the foundational analysis of halo and nearly rectilinear halo orbits [BB79; How84; HC99; Góm+01], and further connects these findings to the symplectic geometry perspective through a Hamiltonian formulation and the use of Moser regularization.

TABLE 1. Summary of the orbit families studied, together with their symmetries and Conley-Zehnder indices. Symmetric orbits are symmetric with respect to $y = 0$, while those marked with r_x are symmetric with respect to $x = 0$.

Orbit Family	System	Symmetries	CZ Index	Section
vertical collision	Hill’s problem	doubly-symmetric	4, 3, 2	4.1
L_1 halo	$\mu \in [0, \mu^*)$	symmetric	4, 3, 2	4.4
	$\mu \in (\mu^*, 0.5)$	symmetric	3, 2	
	Copenhagen	doubly-symmetric	3, 2	
L_2 halo	$\mu \in [0, 0.5]$	symmetric	4, 3	
L_1 halo (collisional)	small $\mu > 0$	symmetric	3, 2	4.2 and 4.3
L_2 halo (collisional)	small $\mu > 0$	symmetric	4	
butterfly	Hill’s problem	doubly-symmetric	7, 8	4.6
	Saturn-Enceladus	symmetric	7, 8	
tri-fly (“left”, “right”)	Hill’s problem	symmetric	11, 12	4.7
	Saturn-Enceladus	symmetric	10, 11, 12	
tri-fly (“up”, “down”)	Hill’s problem	symmetric (r_x)	10, 11	
	Saturn-Enceladus	non-symmetric	10, 11	
W4/W5	Hill’s problem	symmetric (r_x)	3	4.5
	Earth-Moon	non-symmetric	3	
moth	Hill’s problem	doubly-symmetric	4	4.1

For detailed analysis, we compute the Conley-Zehnder indices of the periodic orbit families in this study; the Conley-Zehnder index is a symplectic invariant that remains constant along non-degenerate continuous families and whose change implies bifurcations. This index provides both a diagnostic tool for numerical detection of bifurcations and a topological classification of

families, and has been recently used for numerical bifurcation studies of CR3BP and related systems [Mor+24; AB25; Ayd25]. We give details and computation methods in Appendix D.

The paper is organized as follows. The main text focuses on the underlying celestial mechanics, while the contents of a purely mathematical nature is collected in the appendix. A brief outline is given below. Section 2 introduces the rescaled Hamiltonian formulation for CR3BP and its limiting relation to Hill’s problem. Section 3 presents the numerical framework for Moser regularization and introduces the vertical collision orbit. Section 4 presents the numerical results. In Appendix B, we provide details on Hamiltonians with constraints and the restricted phase space. We follow that in Appendix C with additional details of differential correction in Moser regularization. Appendix D discusses the Conley-Zehnder index and computations of symplectic invariants such as local Floer homology.

2. DYNAMICAL MODELS AND SYMPLECTIC SCALING FRAMEWORK

2.1. The Circular Restricted Three-Body Problem (CR3BP). We consider the *spatial circular restricted three-body problem* (CR3BP), which models the motion of a massless particle in three-dimensional Euclidean space, under the gravitational influence of two massive primary bodies in circular motion. The *mass ratio* of the primaries is denoted by the parameter $\mu \in [0, 1]$.

We choose a rotating coordinate frame fixing the two primaries along the x -axis, the first primary at $e = (-\mu, 0, 0)$ and the second at $m = (1 - \mu, 0, 0)$, and the barycenter of the system at the origin. For our choice of rotation direction, the Hamiltonian of the CR3BP is given by

$$H_\mu(q, p) = \frac{1}{2}|p|^2 + p_1 q_2 - p_2 q_1 - \frac{\mu}{|q - m|} - \frac{1 - \mu}{|q - e|},$$

where the position vector is $q = (q_1, q_2, q_3) \in \mathbb{R}^3$, the momentum vector is $p = (p_1, p_2, p_3) \in \mathbb{R}^3$. The motion of the massless object is described by the Hamilton equations, given by

$$\dot{q} = \partial_p H, \quad \dot{p} = -\partial_q H.$$

We define the Hamiltonian vector field of H_μ as $X_\mu = (\partial_p H, -\partial_q H)$. Due to energy conservation, each trajectory is confined to a five-dimensional energy surface $\Sigma_c = H^{-1}(c)$. The constant c is referred to as the *Jacobi energy*, and the corresponding *Jacobi constant* is given by $\Gamma = -2c$. The system has five equilibrium points, called *Lagrange points*. The three collinear points L_1, L_2, L_3 lie on the q_1 -axis, while the two equilateral points L_4, L_5 form equilateral triangles with the primaries (see Figure 1).

Our main focus is on the dynamics near the second primary, including the region around the collinear points L_1 and L_2 , in the regime where μ is small. This setting is relevant for most planet-moon systems, and is of particular interest for the exploration of icy moons such as Europa orbiting Jupiter and Enceladus orbiting Saturn. Table 2 lists the mass ratios μ of interest in this study, with values from NASA’s Jet Propulsion Laboratory solar system dynamics website: <https://ssd.jpl.nasa.gov>.

System	Mass Ratio (μ)
Earth-Moon	$1.215058560962404 \times 10^{-2}$
Jupiter-Europa	$2.528017528540000 \times 10^{-5}$
Saturn-Enceladus	$1.901109735892602 \times 10^{-7}$

TABLE 2. Table of mass ratio parameters for different three-body systems.

2.2. Hill’s Problem and Symmetries. The Hill’s problem [Hil78] is a limiting case of the CR3BP where the first primary is assumed to be much heavier than the second, and the massless object to be very close to the second primary. The Hamiltonian for the Hill’s problem is given as follows.

$$\hat{H}_0(q, p) = \frac{1}{2}|p|^2 - \frac{1}{|q|} + p_1 q_2 - p_2 q_1 + \frac{1}{2}|q|^2 - \frac{3}{2}q_1^2. \quad (1)$$

We denote the Hamiltonian by \hat{H}_0 because in the next section we will introduce a rescaled Hamiltonian \hat{H}_μ for the CR3BP, which converges to \hat{H}_0 as $\mu \rightarrow 0$. Among the five equilibrium (Lagrange) points in the CR3BP, only the two collinear points L_1 and L_2 remain in the Hill's problem (see Figure 1). Like the CR3BP, the Hill's problem is non-integrable, [MSS05], so numerical methods are essential for studying its detailed dynamics [SS00].

The Hill's problem comes with additional symmetries compared to the CR3BP. In the CR3BP, the Hamiltonian is invariant under the following *reversing symmetries*, which reverse the direction of the Hamiltonian flow:

$$r_y(q_1, q_2, q_3, p_1, p_2, p_3) = (q_1, -q_2, q_3, -p_1, p_2, -p_3), \quad (2)$$

$$r_{yz}(q_1, q_2, q_3, p_1, p_2, p_3) = (q_1, -q_2, -q_3, -p_1, p_2, p_3). \quad (3)$$

In the Hill's problem, two additional reversing symmetries appear:

$$r_x(q_1, q_2, q_3, p_1, p_2, p_3) = (-q_1, q_2, q_3, p_1, -p_2, -p_3), \quad (4)$$

$$r_{xz}(q_1, q_2, q_3, p_1, p_2, p_3) = (-q_1, q_2, -q_3, p_1, -p_2, p_3). \quad (5)$$

Note that the additional symmetries (4) and (5) also appear in the CR3BP in the special case $\mu = 1/2$.

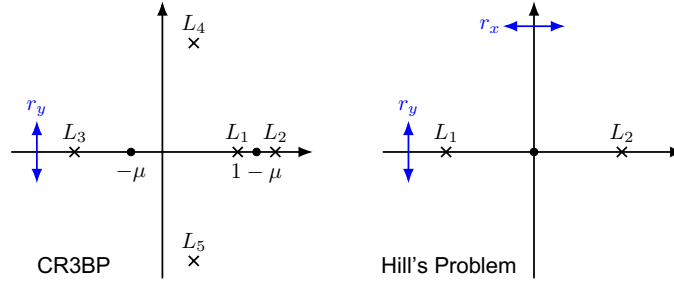


FIGURE 1. Configuration of the Lagrange points and reflection symmetries in the CR3BP (left) and Hill's problem (right). In both models, the reflection symmetry r_y across the plane $y = 0$ is present, while the Hill's problem exhibits additional symmetry r_x across the plane $x = 0$. Only L_1 and L_2 Lagrange points remain in Hill's problem.

2.3. Rescaled CR3BP and the Hill's Limit. We now introduce a rescaled CR3BP Hamiltonian \hat{H}_μ which converges to Hill's problem as $\mu \rightarrow 0$. The derivation follows the descriptions in [MHO09; FvK18] and proceeds through two coordinate transformations. First, we translate the origin to the position of the moon:

$$T(q, p) = (q, p) + m_\mu, \quad m_\mu = (1 - \mu, 0, 0; 0, 1 - \mu, 0).$$

Next, we apply the *symplectic scaling* [MS82]

$$\varphi(q, p) = (\mu^{1/3}q, \mu^{1/3}p),$$

which rescales the Hamilton equations by a constant factor; the *rescaled CR3BP Hamiltonian* is then

$$\hat{H}_\mu(q, p) = \mu^{-2/3} \left((H_\mu \circ T)(\varphi(q, p)) + (1 - \mu) + \frac{(1 - \mu)^2}{2} \right),$$

which expands to

$$\hat{H}_\mu(q, p) = \frac{1}{2}|p|^2 - \frac{1}{|q|} + p_1 q_2 - p_2 q_1 - \frac{1 - \mu}{\mu^{2/3}} \left(\frac{1}{\sqrt{(\mu^{1/3}q_1 + 1)^2 + \mu^{2/3}(q_2^2 + q_3^2)}} + \mu^{1/3}q_1 - 1 \right). \quad (6)$$

We use the hat ($\hat{\cdot}$) notation to indicate the Hamiltonian in scaled coordinates, and h to denote the corresponding energy levels. The energies of the two systems are related by

$$c = \mu^{2/3}h - (1 - \mu) - \frac{(1 - \mu)^2}{2},$$

so that the energy surface $\hat{H}_\mu = h$ corresponds to $H_\mu = c$ under the transformation $\varphi \circ T$ (see Figure 2). As $\mu \rightarrow 0$, we have $c \rightarrow -3/2$, and the Jacobi constants converge to $C = 3$.

In the rescaled Hamiltonian (6), the term in parentheses is $O(\mu^{2/3})$, and \hat{H}_μ is analytic in $\nu = \mu^{1/3}$ at $\mu = 0$. Thus, the limit $\mu \rightarrow 0$ recovers the Hamiltonian for the Hill's problem (1).

Proposition 2.1. *Let \hat{X}_μ be the Hamiltonian vector field of the rescaled CR3BP \hat{H}_μ . For any $\mu_0 \in (0, 1]$, the family $\mu \mapsto \hat{X}_\mu$ defines a one-parameter analytic perturbation (in $\nu = \mu^{1/3}$) of the Hill's problem \hat{X}_0 , in the region $q_1 > -\mu_0^{-1/3}$.*

This rescaling is useful because it provides a perturbative framework where solutions of the Hill's problem continue into the CR3BP. While the expression (6) is not numerically practical due to the singular denominator $\mu^{2/3}$, we provide in Appendix A an equivalent formulation suitable for numerical computations.

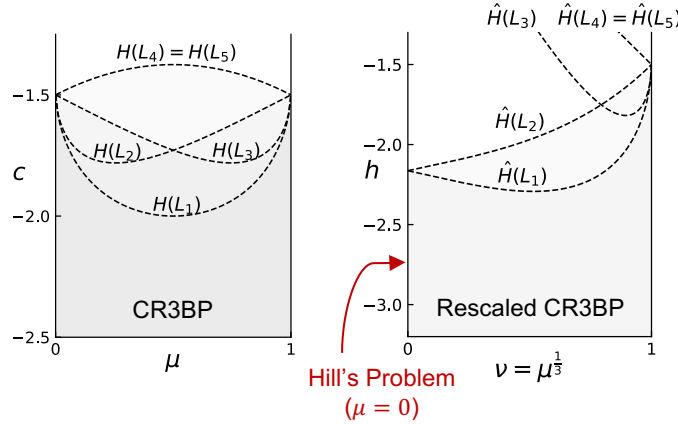


FIGURE 2. Energy levels of the five Lagrange points in the standard CR3BP H_μ (left) and in the rescaled CR3BP \hat{H}_μ (right) as a function of the mass ratio $\mu \in [0, 1]$. In the limit $\mu \rightarrow 0$, the rescaled Hamiltonian corresponds to the Hill's problem \hat{H}_0 , in which only the two collinear Lagrange points L_1 and L_2 remain, both at the same energy level.

Remark 2.2. When $\mu = 1$, the rescaled Hamiltonian \hat{H}_μ corresponds to the *rotating Kepler problem*. Thus, the rescaled CR3BP interpolates between Hill's problem ($\mu \rightarrow 0$) and the rotating Kepler problem ($\mu \rightarrow 1$) in the vicinity of the second primary.

2.4. Non-degeneracy of Periodic and Symmetric Orbits. In the most general setting, we consider a T -periodic solution $\gamma(t)$ of an autonomous Hamiltonian H , where γ lies on the energy level $H = h$. Let $\Sigma = H^{-1}(h)$ denote the energy hypersurface containing γ . Let $\psi : S \rightarrow S$ be the Poincaré return map on a surface of section $S \subset \Sigma$, with $\psi(\gamma(0)) = \gamma(T)$.

We define the appropriate non-degeneracy condition for such orbits as follows.

Definition 2.3. A periodic orbit γ of a Hamiltonian system is said to be *non-degenerate* if the linearized return map satisfies $\det(d\psi - \text{Id}) \neq 0$, i.e., the differential $d\psi$ has no eigenvalue equal to 1.

This condition can be checked numerically using the eigenvalues of the *monodromy matrix* $\Phi = d\varphi^T(\gamma(0))$, where φ^t denotes the time t -flow of the Hamiltonian vector field X_H . These eigenvalues are referred to as the *Floquet multipliers*.

Lemma 2.4. *A periodic orbit γ is non-degenerate if and only if its monodromy matrix Φ has exactly two eigenvalues equal to 1.*

Proof. See [MZ05, Lemma 2.3]. \square

We now introduce a suitable non-degeneracy condition for symmetric periodic orbits. Let r be a *reversing symmetry* of the Hamiltonian, satisfying

$$H \circ r = H, \quad r \circ \varphi^t = \varphi^{-t} \circ r,$$

where φ^t denotes the Hamiltonian flow. We consider the case where r is an involution, i.e. $r^2 = \text{id}$. The fixed-point set

$$\text{Fix}(r) = \{x \in \mathbb{R}^6 \mid r(x) = x\}$$

has half the dimension of the phase space. An *r-symmetric periodic orbit* of period T satisfies

$$r(\gamma(t)) = \gamma(-t), \quad \text{so that } \gamma(0), \gamma(T/2) \in \text{Fix}(r).$$

Let $S \subset \Sigma$ be a surface of section such that $r(S) = S$ and $\text{Fix}(r) \cap \Sigma \subset S$, and assume

$$\psi(\gamma(0)) = \gamma(T/2).$$

At each $x \in \text{Fix}(r) \cap \Sigma$, the tangent space decomposes into the eigenspaces of dr :

$$T_x S = E_1 \oplus E_{-1}, \quad (dr|_S)|_{E_{\pm 1}} = \pm \text{id},$$

where E_1 corresponds to directions tangent to $\text{Fix}(r) \cap \Sigma$.

Definition 2.5. The symmetric orbit γ is *non-degenerate as an r-symmetric periodic orbit* if for every nonzero $v \in E_1$,

$$(d\psi(v))_{E_{-1}} \neq 0,$$

i.e. the image of E_1 under $d\psi$ has a nontrivial component in E_{-1} .

Lemma 2.6. *If a symmetric periodic orbit γ is non-degenerate (i.e. $\det(d\psi^2 - \text{id}) \neq 0$), then it is also non-degenerate as an r-symmetric orbit.*

Proof. Suppose instead that $d\psi(v) \in E_1$ for some $v \in E_1 \setminus 0$, so that $dr \circ d\psi(v) = d\psi(v)$. Since $\psi \circ r \circ \psi = r$, we have

$$d\psi^2(v) = d\psi \circ dr \circ d\psi(v) = dr(v) = v.$$

Thus v is an eigenvector of $d\psi^2$ with eigenvalue 1, implying that the periodic orbit is degenerate, which is a contradiction. \square

2.5. Perturbation of Periodic Orbits from Hill's Problem to CR3BP. Applying Poincaré's perturbation theory of periodic orbits, we describe how non-degenerate periodic orbits of the Hill's problem persist in the CR3BP for small mass ratios. Closely related approach is the method of *generating solutions* studied in the works of Perko, Hénon, Bruno, and Varin [Per83; Hén97; BV07], which continues planar symmetric orbits of Hill's problem to the CR3BP within the perturbative framework. Here, we state a general perturbative result (Theorem 2.7) on fixed energy surfaces, with leading-order approximations which will be used for numerical continuation of these solutions.

Theorem 2.7. *Let γ_0 be a non-degenerate periodic orbit of the Hill's problem (Hamiltonian \hat{H}_0) with period T_0 and energy $\hat{H}_0 = h$. Then, for sufficiently small $\mu > 0$, there exists a smooth family of periodic orbits γ_μ of the CR3BP with the following properties:*

- (1) *The location x_μ of γ_μ on a surface of section satisfies:*

$$x_\mu - m_\mu = \mu^{-1/3} x_0 + O(\mu^{2/3}),$$

where $m_\mu = (1 - \mu, 0, 0; 0, 1 - \mu, 0)$.

- (2) *The period of γ_μ satisfies: $T_\mu = T_0 + O(\mu^{1/3})$.*

- (3) *The Jacobi energy of γ_μ is given by:*

$$c(\mu) = \mu^{2/3} h - (1 - \mu) - \frac{(1 - \mu)^2}{2}.$$

- (4) The Floquet multipliers of γ_μ change continuously with respect to μ .
 (5) If the orbit γ_0 is symmetric with respect to (2) or (3), then the perturbed orbit γ_μ is also symmetric.

Proof. We apply perturbation theory of periodic orbits (see [MZ05, Theorem 2.2] or [MHO09, Section 9.1]) to the fixed energy surface $\hat{H}_\mu^{-1}(h)$ of the rescaled CR3BP Hamiltonian \hat{H}_μ . Let $\nu = \mu^{1/3}$, and consider a Poincaré return map $\psi(x; \nu)$ defined on a surface of section $S \subset \hat{H}_\mu^{-1}(h)$ through a point $x(0)$ on the orbit γ_0 . We seek a family of fixed points $x(\nu)$ such that

$$x(\nu) = \psi(x(\nu); \nu).$$

By the non-degeneracy assumption, we have that

$$\frac{d\psi}{dx}(x(0); 0) - \text{Id}$$

is non-singular. Thus, by the implicit function theorem, such $x(\nu)$ exists for small $\nu > 0$ and is analytic with respect to ν .

This gives a family $\hat{\gamma}_\mu$ of periodic solutions of the rescaled CR3BP Hamiltonian \hat{H}_μ for small ν , starting from the original orbit γ_0 of the Hill's problem. Its return time T is also defined implicitly by $\varphi^T(x; \nu) \in S$, where φ^T is denotes the time- T flow, and hence is analytic with respect to x and ν . Transforming the family $\hat{\gamma}_\mu$ back to the original CR3BP coordinates gives the desired family γ_μ . Continuity of the Floquet multipliers follows from the smooth dependence of the linearized return map $d\varphi^T$ on ν .

In the case where γ_0 is symmetric, Lemma 2.6 ensures that it is non-degenerate as a symmetric periodic orbit. The same implicit function theorem argument then yields a smooth family of symmetric periodic orbits γ_μ . \square

Remark 2.8. The perturbation result also applies to symmetric periodic orbits that are non-degenerate as symmetric periodic orbits, even if they are degenerate as ordinary periodic orbits. An example of this will be discussed in Section 4.2.

2.6. Numerical Continuation with respect to Mass Parameter. The leading-order approximations of Theorem 2.7 provide initial guesses for numerically continuing periodic orbits when the mass ratio is small. This continuation can be carried out from Hill's problem to the CR3BP, or vice versa, or between CR3BP systems with different small mass ratios. We make the latter precise in the following corollary.

Corollary 2.9. *Consider two small mass ratios $\mu_1 > \mu_2 > 0$. Let γ_1 be a periodic orbit in the CR3BP system H_{μ_1} with mass ratio μ_1 , with Jacobi energy c_1 and period T_1 , assumed to be a continuation from Hill's problem as in Theorem 2.7. Then there exists a corresponding periodic orbit γ_2 for H_{μ_2} :*

- (1) The location x_2 of γ_2 on a surface of section satisfies:

$$x_2 - m_2 = (x_1 - m_1) \cdot \left(\frac{\mu_2}{\mu_1} \right)^{1/3} + O(\mu_1^{1/3} \mu_2^{1/3}),$$

where $m_i = (1 - \mu_i, 0, 0; 0, 1 - \mu_i, 0)$ for $i = 1, 2$.

- (2) The period is given by: $T_2 = T_1 + O(\mu_1^{1/3})$.

- (3) The Jacobi energy is:

$$c_2 = \mu_2^{2/3} h - (1 - \mu_2) - \frac{(1 - \mu_2)^2}{2}, \quad \text{where} \quad h = \mu_1^{-2/3} \left(c_1 + (1 - \mu_1) + \frac{(1 - \mu_1)^2}{2} \right).$$

This scaling provides a practical method for predicting periodic orbits at a nearby mass ratio $\mu = \mu_{\text{prev}} + \Delta\mu$ from a known orbit at μ_{prev} . The Jacobi energy c is updated via the intermediary Hill energy h , computed by

$$h = \mu_{\text{prev}}^{-2/3} \left(c_{\text{prev}} + (1 - \mu_{\text{prev}}) + \frac{(1 - \mu_{\text{prev}})^2}{2} \right), \quad c = \mu^{2/3} h - (1 - \mu) - \frac{(1 - \mu)^2}{2}.$$

The initial point is rescaled as

$$X - m_\mu = (X_{\text{prev}} - m_{\mu_{\text{prev}}}) \cdot \left(\frac{\mu}{\mu_{\text{prev}}} \right)^{1/3},$$

and the period remains unchanged to leading order: $T = T_{\text{prev}}$. The resulting prediction is then refined using a shooting method with Newton-type correction that ensures periodicity at the updated parameters. This process is summarized in Algorithm 1. We shall use this continuation for computation of bifurcation surfaces, i.e. bifurcation graphs of halo orbits and vertical collision orbits for the range $\mu \in [0, 0.5]$ in Section 4.4.

Algorithm 1: Scaling Continuation Across Small Mass Ratios

Input: Periodic orbit $(X_{\text{prev}}, T_{\text{prev}}, c_{\text{prev}})$ at μ_{prev} , step size $\Delta\mu$

Output: Periodic orbit (X, T, c) at $\mu = \mu_{\text{prev}} + \Delta\mu$

$\mu \leftarrow \mu_{\text{prev}} + \Delta\mu;$

$h \leftarrow \mu_{\text{prev}}^{-2/3} \left(c_{\text{prev}} + (1 - \mu_{\text{prev}}) + \frac{(1 - \mu_{\text{prev}})^2}{2} \right);$

$c \leftarrow \mu^{2/3} h - (1 - \mu) - \frac{(1 - \mu)^2}{2};$

$X \leftarrow m_\mu + (X_{\text{prev}} - m_{\mu_{\text{prev}}}) \cdot (\mu / \mu_{\text{prev}})^{1/3};$

$T \leftarrow T_{\text{prev}};$

Correct (X, T) using differential correction at fixed Jacobi energy c ;

return $(X, T, c);$

The correction at fixed Jacobi energy is implemented using a single-shooting scheme on a chosen Poincaré section. For clarity, we describe the case of the section $q_2 = 0$, but an analogous scheme on the section $p_3 = 0$ is used in Section 4.5. Let q_1, q_3, p_1, p_3 be the coordinates of a predicted initial condition and T be a predicted period. The missing momentum p_2 is obtained by solving the quadratic equation $H(q, p) = c$ for p_2 . We also compute its derivatives $\frac{\partial p_2}{\partial q_1}, \dots, \frac{\partial p_2}{\partial p_3}$. The periodicity condition is expressed as finding zeros of the map

$$F(q_1, q_3, p_1, p_3, T) = \pi_{(q_1, q_2, q_3, p_1, p_3)} \circ \varphi^T(q_1, 0, q_3, p_1, p_2, p_3) - (q_1, 0, q_3, p_1, p_3)$$

where φ^t denotes the Hamiltonian flow and π is the projection onto the listed coordinates². Starting from an initial guess $X_0 = (q_1, q_3, p_1, p_3, T)$, we apply Newton iterations

$$X_{i+1} = X_i - [DF(X_i)]^{-1} F(X_i)$$

until convergence, where a vector X_i is considered to be a periodic orbit if $|F(X_i)| < 10^{-10}$. The computation of Jacobian $DF(X_i)$ involves the linearized flow $d\varphi^T$, which is obtained by integrating the first-order variational equations along the trajectory.

3. MOSER REGULARIZATION

In this section, we develop a numerical framework for detection and continuation of periodic orbits in the Moser regularized circular restricted three-body problem (CR3BP). These methods will be essential for the numerical study of families of collision and near-collision spatial orbits and their bifurcation graphs.

3.1. Moser's Transformation. We describe Moser's transformation of coordinates $(q, p) \in \mathbb{R}^3 \times \mathbb{R}^3$ to the cotangent bundle T^*S^3 of the unit 3-sphere:

$$T^*S^3 = \{(\xi, \eta) \in \mathbb{R}^4 \times \mathbb{R}^4 \mid |\xi|^2 = 1, \xi \cdot \eta = 0\}.$$

²The period T is included in the map F , because the k -th arrival time at the Poincaré section may be discontinuous in the perturbation parameter.

To define the transformation, we first switch the roles of position and momentum coordinates through the switch map $(x, y) = (p, -q)$. Moser's transformation is then given by:

$$\begin{aligned} \xi_0 &= \frac{|x|^2 - 1}{|x|^2 + 1}, & \xi_k &= \frac{2x_k}{|x|^2 + 1}, & k &= 1, 2, 3. \\ \eta_0 &= x \cdot y, & \eta_k &= \frac{|x|^2 + 1}{2} y_k - (x \cdot y) x_k, & k &= 1, 2, 3. \end{aligned} \quad (7)$$

Note that here the momentum $x \in \mathbb{R}^3$ is mapped to the unit 3-sphere $S^3 \subset \mathbb{R}^4$ using the inverse stereographic projection, where the singularity $p = \infty$ corresponds to $\xi_0 = 1$, i.e. the north pole N of the sphere. Figure 3 shows a schematic picture of the transformation. The inverse of this transformation is given as follows:

$$q_k = y_k = \eta_0 \xi_k + (1 - \xi_0) \eta_k, \quad p_k = -x_k = -\frac{\xi_k}{1 - \xi_0}, \quad k = 1, 2, 3.$$

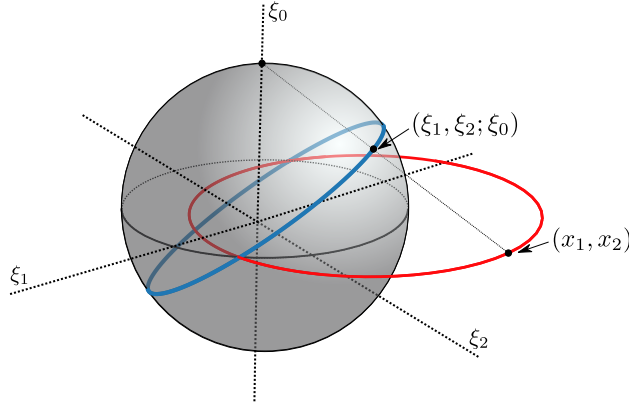


FIGURE 3. Schematic picture of Moser regularization, where the momentum curve (also known as a *hodograph*) of an orbit is mapped to a unit sphere. The figure shows the case for the planar problem, where the unregularized momentum coordinates (x_1, x_2) are mapped to (ξ_0, ξ_1, ξ_2) on the sphere via inverse stereographic projection, with ξ_0 representing the vertical axis. Collision orbits correspond to trajectories passing through the north pole $\xi_0 = 1$, and the position coordinates correspond to tangent vectors at each point.

3.2. Moser Regularization of CR3BP and Hill's Problem. In Moser's work [Mos70], the transformation (7) was introduced to regularize the singularity of the Kepler problem. Here, we consider the regularization of Hamiltonian systems of the form

$$H(q, p) = \frac{1}{2}|p|^2 + p_1 q_2 - p_2 q_1 - \frac{g}{|q|} + \tilde{V}(q),$$

at the singularity at $q = 0$, where $g \neq 0$ is a constant and \tilde{V} is analytic in a neighborhood of $q = 0$. After an appropriate coordinate translation that places the singularity at the origin, this general form includes the CR3BP Hamiltonian H_μ , the rescaled CR3BP Hamiltonian \hat{H}_μ , and the Hill's problem \hat{H}_0 . The constant g equals μ for the CR3BP and 1 for Hill's problem. For a general description of the Moser regularization in Stark-Zeeman systems, see [CFvK17].

To define the regularized Hamiltonian, we first set

$$K(q, p) = (H - c)|q| = \left(\frac{1}{2}(|p|^2 + 1) - (c + 1/2) + p_1 q_2 - p_2 q_1 + \tilde{V}(q) \right) |q| - g.$$

The energy level set $H = c$ now corresponds to $K = 0$, and the dynamics on this energy surface is reparametrized by $X_K = |q|X_H$. In the regularized coordinates (ξ, η) , we have

$$K(\xi, \eta) = \left(1 - (1 - \xi_0)(c + 1/2) + (1 - \xi_0)(\xi_2 \eta_1 - \xi_1 \eta_2) + (1 - \xi_0)\tilde{V}(\xi, \eta) \right) |\eta| - g.$$

Finally, we smooth this to define the *Moser regularized Hamiltonian*

$$Q : T^*S^3 \rightarrow \mathbb{R}, \quad Q(\xi, \eta) = \frac{1}{2g}(K(\xi, \eta) + g)^2.$$

The energy level set $K = 0$ corresponds to $Q = \frac{g}{2}$, where the dynamics is preserved via $X_Q = X_K$. The following summarizes the result.

Proposition 3.1. *A trajectory $\gamma(t)$ of the unregularized dynamics X_H in energy level $H = c$ corresponds to the trajectory $\tilde{\gamma}(\tau)$ of the Moser regularized dynamics X_Q in energy level $Q = \frac{g}{2}$ via the transformation (7) and time reparametrization $t = \int_0^\tau |q| d\tau$.*

The Moser regularization gives dynamics on the *restricted phase space* $T^*S^3 \subset \mathbb{R}^8$ defined by the two constraints:

$$f_1 = |\xi|^2 - 1 = 0, \quad f_2 = \xi \cdot \eta = 0.$$

The corresponding Hamiltonian vector field on T^*S^3 is obtained as follows.

Lemma 3.2. *The Hamiltonian vector field of Q on T^*S^3 is given by*

$$X_Q = \tilde{X}_Q - \frac{\{f_2, Q\}}{\{f_2, f_1\}} X_{f_1} - \frac{\{f_1, Q\}}{\{f_1, f_2\}} X_{f_2},$$

where $\tilde{X}_Q = (\partial_p Q, -\partial_q Q)$ denotes the Hamiltonian vector field of Q in the ambient space $\mathbb{R}^4 \times \mathbb{R}^4$.

In Appendix B, we give a general formulation of restricted phase spaces with $2k$ constraints, and the proof of the formula for X_Q in this generalized setting.

Remark 3.3. The vector field X_Q refers to the *intrinsic* Hamiltonian vector field of Q on the restricted phase space T^*S^3 as defined above. In contrast, $\tilde{X}_Q := (\partial_p Q, -\partial_q Q)$ is the *extrinsic* Hamiltonian vector field of Q viewed as a function on the ambient space $\mathbb{R}^4 \times \mathbb{R}^4$. For numerical integration, we work in \mathbb{R}^8 and compute X_Q from the extrinsic vector field \tilde{X}_Q using Lemma 3.2. The regularized dynamics is then given by the ODEs

$$(\dot{\xi}, \dot{\eta}) = X_Q(\xi, \eta). \quad (8)$$

3.3. Floquet Multipliers and Bifurcations. A key advantage of the Moser regularization is that the Floquet multipliers of periodic orbits can be computed in a simple way. Let γ be a periodic orbit of period τ in the unregularized system, and let $\tilde{\gamma}$ be the corresponding periodic orbit in the regularized system on $T^*S^3 \subset \mathbb{R}^8$.

Consider the monodromy matrix $\tilde{\Phi} = d\tilde{\varphi}_\tau(\tilde{\gamma}(0))$ of the flow of X_Q in \mathbb{R}^8 . Because this flow has two additional integrals f_1 and f_2 , we can take a basis adapted to these two integrals and to the tangent space of T^*S^3 , for which the monodromy matrix takes the block form

$$\left(\begin{array}{c|c} \text{id}_2 & 0 \\ \hline * & S \end{array} \right),$$

where S represents the derivative of the flow restricted to T^*S^3 (see Lemma 2.3 of [MZ05]). The matrix S is symplectic and is conjugate to the monodromy matrix of γ in the original coordinates via the derivative of Moser's transformation (7). Thus the nontrivial Floquet multipliers of γ and $\tilde{\gamma}$ are the same.

Lemma 3.4. *Let γ be a periodic orbit in the unregularized system X_H with Floquet multipliers $1, 1, \lambda_1, \dots, \lambda_4$. Then the Floquet multipliers of the corresponding orbit $\tilde{\gamma}$ in the Moser regularization are given as*

$$1, 1, 1, 1, \lambda_1, \dots, \lambda_4.$$

If more than four eigenvalues are equal to 1, the orbit is degenerate and bifurcations may occur. Let X_s be a smooth family of vector fields, and let $s \mapsto \gamma_s$ be a smooth one-parameter family of periodic orbits of X_s . The linearized return map R_s then depends smoothly on s , and its eigenvalues can be chosen to vary continuously with s . In Hamiltonian systems, these eigenvalues lie on the real axis \mathbb{R} or on the unit circle $S^1 \subset \mathbb{C}$. Hence, changes in stability may occur when a pair of eigenvalues merges at 1 (*tangent bifurcation*), at -1 (*period-doubling*).

bifurcation), or when two pairs collide on S^1 and leave the unit circle as a complex quadruple (*Krein collision*) [HM87]. Below we describe the local bifurcations relevant to our study, following the terminology of [Cam99].

Definition 3.5 (Local Bifurcations of Periodic Orbits). A parameter value s_0 is called a

- (1) **tangent bifurcation** if an eigenvalue family λ_s satisfies $\lambda_s \in S^1$ for $s < s_0$ and $\lambda_s \in \mathbb{R}_{>0}$ for $s > s_0$;
- (2) **fold bifurcation** if two smooth families of periodic orbits γ_s and γ'_s coincide at $s = s_0$, with respective eigenvalues λ_s and λ'_s satisfying $\lambda_s \in S^1$ and $\lambda'_s \in \mathbb{R}_{>0}$ for $s < s_0$;
- (3) **period-doubling bifurcation** if an eigenvalue family λ_s satisfies $\lambda_s \in S^1$ for $s < s_0$ and $\lambda_s \in \mathbb{R}_{<0}$ for $s > s_0$;
- (4) **secondary Hopf bifurcation** if two eigenvalue families λ_s, μ_s lie in $S^1 \setminus \{1, -1\}$ and are distinct for $s < s_0$, while $\lambda_s, \mu_s \in \mathbb{C} \setminus S^1$ for $s > s_0$;
- (5) **modified secondary Hopf bifurcation** if two eigenvalue families $\lambda_s, \mu_s \in \mathbb{R} \setminus \{1, -1\}$ and are distinct for $s < s_0$, while $\lambda_s, \mu_s \in \mathbb{C} \setminus \mathbb{R}$ for $s > s_0$.

Note that the modified secondary Hopf bifurcation does not involve a change in stability.

3.4. Differential Correction and Continuation. We present a differential correction scheme formulated directly in the Moser regularized coordinates (7), which allows periodic orbits to be continued smoothly through collision configurations. The Poincaré section is chosen as $\xi_3 = 0$, corresponding to $p_3 = 0$ in the unregularized coordinates. This section naturally captures turning points in the z -direction, such as the periapsis and apoapsis of halo orbits, and contains the fixed-point locus of the symmetries. All numerical integrations are performed using the high-order Taylor integrator implemented in the `heyoka` library [BI21].

We choose the vector of free variables

$$X = (\xi_1, \xi_2, \eta_1, \eta_2, \tau),$$

where τ is the (predicted) period of the orbit. Given X , we consecutively determine the ξ_0 and η_0 variables based on the constraints $|\xi|^2 = 1$ and $\xi \cdot \eta = 0$, respectively. Then, η_3 is determined by solving the energy constraint $Q = 1/(2g)$, for which we use numerical root finding based on Brent's method [Bre71]. Define the constraint function:

$$F(X) = p \circ \varphi^\tau(\xi_0, \xi_1, \xi_2, 0; \eta_0, \eta_1, \eta_2, \eta_3) - (\xi_1, \xi_2, 0, \eta_1, \eta_2), \quad (9)$$

where φ^τ denotes integration of the flow of X_Q for time τ , and p is the projection to $(\xi_1, \xi_2, \xi_3, \eta_1, \eta_2)$ coordinates. The differential correction scheme is given by Newton's method as follows:

$$X_{i+1} = X_i - DF(X_i)^{-1} F(X_i), \quad i = 0, 1, 2, \dots$$

We iterate until convergence, where a vector X_i is considered to be a periodic orbit if $|F(X_i)| < 10^{-10}$. To compute the Jacobian matrix DF , we evaluate the linearized flow, as well as symbolically compute the derivatives of the dependent variables ξ_0, η_0 and η_3 with respect to the free variables. See Appendix C for the details of this derivation.

We describe the correction scheme for symmetric periodic orbits with respect to the reflection r_y across the plane $y = 0$; the formulation for the reflection r_x across $x = 0$ is analogous. For this symmetry, the fixed point locus is given by $q_2 = p_1 = p_3 = 0$, which in Moser coordinates corresponds to $\xi_1 = \xi_3 = \eta_0 = \eta_2 = 0$. We can therefore reduce the free variable vector to

$$X_{\text{sym}} = (\xi_2, \eta_1, \tau).$$

The remaining variables ξ_0 and η_3 are determined as before. The constraint function is then defined as

$$F_{\text{sym}}(X_{\text{sym}}) = p_{\text{sym}} \circ \varphi^\tau(\xi_0, 0, \xi_2, 0; 0, \eta_1, 0, \eta_3),$$

where p_{sym} projects to (ξ_1, ξ_3, η_0) coordinates. This gives a reduced 3-dimensional correction scheme.

For the continuation of periodic orbits, we apply pseudo-arclength continuation [Kuz23, Section 10.2.1] in the unregularized system, while in the Moser regularized system we perform natural parameter continuation with respect to the Hamiltonian energy.

3.5. Vertical Collision Orbits. Vertical collision orbits in the Hill's problem arise from dynamics confined to the z -axis, i.e. the submanifold $q_1 = q_2 = p_1 = p_2 = 0$, which is invariant under the Hamiltonian flow. Restricting to the z -axis, we get a reduced 2-dimensional Hamiltonian system on the (q_3, p_3) -plane:

$$\dot{q}_3 = \frac{\partial \hat{H}_0}{\partial p_3} = p_3, \quad \dot{p}_3 = -\frac{\partial \hat{H}_0}{\partial q_3} = -\frac{q_3}{|q_3|^3} - q_3.$$

This system is singular at $q_3 = 0$, corresponding to collision with the primary at the origin. For initial conditions with $q_3 \neq 0$, the trajectory reaches a collision after a finite time, which is computed in [BFvK19].

To continue these trajectories through collision, we apply Moser regularization. In this framework, the dynamics restricted to the vertical subspace corresponds to the invariant set

$$\begin{aligned} \xi_1 &= \xi_2 = \eta_1 = \eta_2 = 0, \\ \xi_0^2 + \xi_3^2 &= 1, \\ \xi_0 \eta_0 + \xi_3 \eta_3 &= 0, \end{aligned}$$

giving a one degree-of-freedom Hamiltonian system. The regularized Hamiltonian on this subset takes the form

$$Q = \frac{1}{2} \left(1 - (1 - \xi_0)(c + 1/2) + (1 - \xi_0) \cdot \frac{1}{2} (\eta_0 \xi_3 + (1 - \xi_0) \eta_3)^2 \right)^2 (\eta_0^2 + \eta_3^2)^2. \quad (10)$$

This function is smooth across the collision locus $p_3 = \pm\infty$, which corresponds to $\xi_0 = 1$. Thus, the collision trajectories extend to smooth periodic orbits in the regularized phase space, as shown in Figure 4. We call these orbits *vertical collision orbits*.

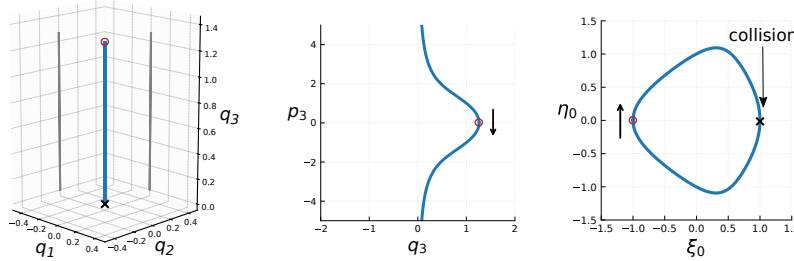


FIGURE 4. Northern vertical collision orbit in Hill's problem, shown in configuration space (left), the (q_3, p_3) plane (center), and Moser-regularized coordinates (ξ_0, η_0) (right). Red marker denotes apoapsis (maximum q_3), and the cross indicates the periapsis corresponding to collision with the light primary.

For each energy level $\hat{H}_0 = h$, there exists a unique pair of vertical collision orbits. These can be characterized explicitly using the Poincaré section $p_3 = 0$, at which the corresponding position q_3 is given by

$$\hat{H}_0 = -\frac{1}{|q_3|} + \frac{1}{2} q_3^2 = h. \quad (11)$$

Solving for q_3 , we get two solutions for each h with opposite signs, corresponding to two orbits reflected about the origin. We refer to the orbit with $q_3 > 0$ as the *northern* vertical collision orbit, and the other with $q_3 < 0$ *southern*. The positive solution $q_{3,\max}$ represents the maximal height of these orbits, and increases monotonically with energy h , starting from zero and increasing to infinity.

Proposition 3.6. *For each energy level $\hat{H}_0 = h$, the Moser regularized Hill's problem admits a pair of vertical collision orbits $\gamma_{\pm,h}$ whose motion is confined to the z -axis, with initial coordinates*

$$\gamma_{\pm,h}(0) = (\pm q_{3,\max}(h), 0, 0; 0, 0, 0)$$

where $q_{3,\max}(h)$ is the positive solution to equation (11).

Remark 3.7. For numerical computation of vertical collision orbits, we first solve equation (11) for q_3 using Cardano's formula:

$$q_{3,\max} = \frac{1}{3} \sqrt[3]{27 + 3\sqrt{-24h^3 + 81}} + 2 \frac{h}{\sqrt[3]{27 + 3\sqrt{-24h^3 + 81}}}.$$

The resulting initial condition can then be integrated in the regularized system until the second return to the section $\xi_3 = 0$, which corresponds to $p_3 = 0$.

4. NUMERICAL RESULTS

4.1. Bifurcations of Vertical Collision Orbits and Halo Orbits in Hill's Problem. The bifurcation diagram of the northern vertical collision family is shown in Figure 5. As a one-parameter family parameterized by the Hamiltonian energy $\dot{H}_0 = h$, the family begins as a linearly stable periodic orbit possessing two pairs of elliptic Floquet multipliers. As h increases, five distinct bifurcation events are detected:

- (1) **First period-doubling bifurcation** ($h \approx -1.02$) A period-doubling bifurcation occurs as an elliptic pair of Floquet multipliers transitions to a hyperbolic pair, at which point a doubly symmetric *butterfly family* of periodic orbits emerges.
- (2) **First pitchfork bifurcation** ($h \approx -0.85$) The remaining elliptic pair transitions to a positive hyperbolic pair at a point of a pitchfork bifurcation. This bifurcation gives rise to two branches of r_y -symmetric orbits, which appear in symmetry with respect to the reflection r_x . These correspond to the northern L_1 and L_2 halo families.
- (3) **Second pitchfork bifurcation** ($h \approx 0.04$) A second pitchfork bifurcation occurs, producing two branches of r_x -symmetric orbits that appear in symmetry with respect to the reflection r_y . After perturbation to the CR3BP, the r_x -symmetry of the orbits is broken, giving families of non-symmetric orbits which connect to vertical families of orbits emanating from the L_4 and L_5 Lagrange points. These correspond to the W4/W5 families described in [Doe+07].
- (4) **Second period-doubling bifurcation** ($h \approx 0.09$) A second period-doubling bifurcation occurs, giving rise to the “moth” family of doubly symmetric orbits.
- (5) **Secondary Hopf bifurcation** ($h \approx 0.11$) Finally, a secondary Hopf bifurcation is observed, in which two pairs of Floquet multipliers collide on the unit circle and move off into the complex plane. This transition marks the onset of strong instability, with the modulus of one pair increasing far beyond unity while the other decreases toward zero.

The branches described in (1)-(4) are illustrated in Figure 6.

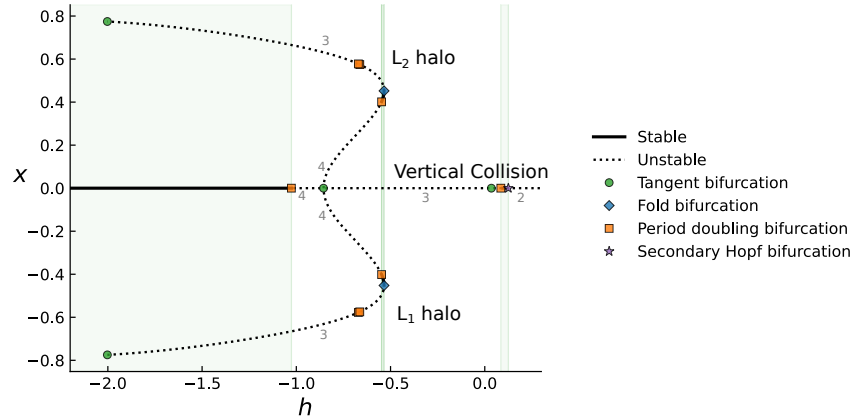


FIGURE 5. Bifurcation diagram of the vertical collision orbit (central line) and the L_1 and L_2 halo families (branches) in Hill's problem. The horizontal axis corresponds to the Hamiltonian energy $\dot{H}_0 = h$, and the vertical axis shows the x -coordinate at the apoapsis.

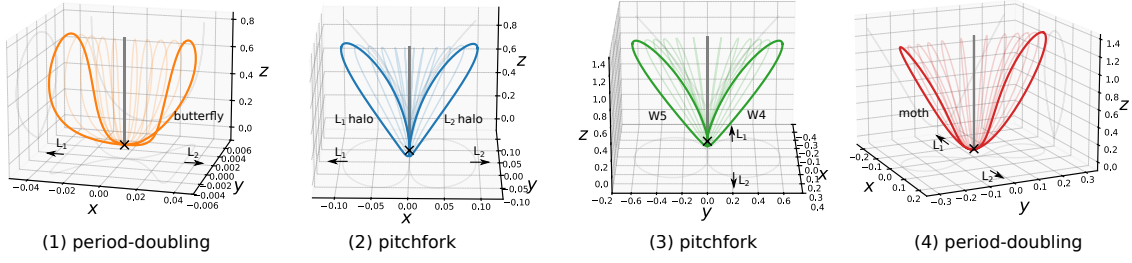


FIGURE 6. Periodic orbit families bifurcating from vertical collision orbits (gray) in Hill's problem: (1) butterfly family from the first period-doubling bifurcation; (2) L_1 and L_2 halo families from the first pitchfork bifurcation; (3) r_x -symmetric branches from the second pitchfork bifurcation; (4) doubly symmetric family from the second period-doubling bifurcation.

The bifurcation graphs of the two halo branches are plotted together in Figure 5. The halo families originate from the planar Lyapunov family at $h \approx -2.0$. As the energy increases, each halo branch undergoes two successive period-doubling bifurcations followed by a fold bifurcation. In the literature, this fold bifurcation is often associated with the onset of the *nearly rectilinear halo orbit* (NRHO) regime [ZHD20]. Beyond the fold, the family undergoes a narrow interval of linear stability that terminates at another period-doubling bifurcation. Continuing further in h , the family connects with the vertical collision orbit at the pitchfork bifurcation near $h \approx -0.85$. In Figure 7 we visualize the northern L_1 halo family as it bifurcates from the planar Lyapunov orbit and terminates in the vertical collision orbit.

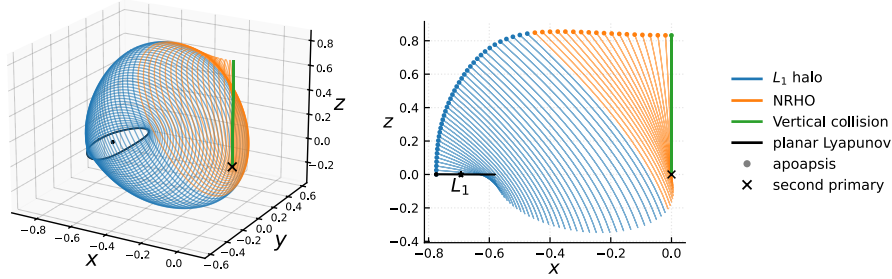


FIGURE 7. Continuation of the L_1 halo family in Hill's problem, from its bifurcation from the planar Lyapunov orbit to its termination in the vertical collision orbit.

4.2. Perturbation of Vertical Collision Orbits to CR3BP. We study the continuation of the vertical collision orbits of Hill's problem under perturbation to CR3BP, with respect to the parameter $\nu = \mu^{1/3}$. The discussion here generalizes the similar description given for the KS regularization in [Góm+01, Section 2.3.6].

Fix a Hamiltonian energy $\hat{H}_\nu = h$ and let X_ν denote the Hamiltonian vector field on the Moser regularized energy surface. Denote by $\varphi_\nu(x, t)$ the time- t flow of X_ν . Let x_0 be a point of the vertical collision orbit of Hill's problem on the Poincaré section $\xi_3 = 0$, with period t_0 . We seek perturbed solutions (x_ν, t_ν) satisfying

$$\varphi_\nu(x_\nu, t_\nu) - x_\nu = 0. \quad (12)$$

The constraints on x_ν include the energy surface $\hat{H}_\nu = h$, the section $\xi_3 = 0$, and the constraints $f_1 = |\xi|^2 = 1$ and $f_2 = \xi \cdot \eta = 0$ from the Moser regularization.

Linearizing with respect to ν at $\nu = 0$ gives

$$(d\varphi_0 - \text{id})\Delta x + X_0(x_0)\Delta t + \Delta\varphi = 0, \quad (13)$$

where $\Delta x = \frac{dx_\nu}{d\nu}|_{\nu=0}$, $\Delta t = \frac{dt_\nu}{d\nu}|_{\nu=0}$, and

$$\Delta\varphi = \int_0^{t_0} \frac{\partial X_0}{\partial \nu}(\varphi_0(x_0, s)) ds. \quad (14)$$

Since the vertical collision orbit lies in the invariant “vertical” subspace $\xi_1 = \xi_2 = \eta_1 = \eta_2 = 0$, we project (13) onto the “horizontal” coordinates $(\xi_1, \xi_2, \eta_1, \eta_2)$. In this projection, the Δt term vanishes, yielding

$$A \begin{bmatrix} \Delta\xi_1 \\ \Delta\xi_2 \\ \Delta\eta_1 \\ \Delta\eta_2 \end{bmatrix} + b = 0, \quad (15)$$

where

$$A = \frac{\partial(\pi_{(\xi_1, \xi_2, \eta_1, \eta_2)} \circ \varphi_0)}{\partial(\xi_1, \xi_2, \eta_1, \eta_2)} - \text{id}, \quad b = \pi_{(\xi_1, \xi_2, \eta_1, \eta_2)}(\Delta\varphi). \quad (16)$$

The matrix A is invertible except at two energy levels $h_1 \approx -0.85$ and $h_2 \approx 0.04$ corresponding to degeneracies. Numerical evaluation shows that the solutions $\Delta x = -A^{-1}b$ diverges near $h = h_1$, but is continuous near $h = h_2$, with $\Delta\xi_1 = \Delta\eta_2 = 0$, implying perturbation to symmetric orbits.

Next, we consider the r_y -symmetric continuation of the vertical collision orbits. We look for perturbed r_y -symmetric solutions (x_ν, t_ν) satisfying

$$\pi_{(\xi_1, \xi_3, \eta_0, \eta_2)} \circ \varphi_\nu(x_\nu, t_\nu) = 0 \quad (17)$$

while restricting to the fixed point locus

$$x_\nu \in \text{Fix}(r_y) = \{(\xi, \eta) \mid \xi_1 = \xi_3 = \eta_0 = \eta_2 = 0\}.$$

The linearized perturbation projected onto (ξ_2, η_1) coordinates give

$$A_{\text{sym}} \cdot \begin{bmatrix} \Delta\xi_2 \\ \Delta\eta_1 \end{bmatrix} + b_{\text{sym}} = 0, \quad (18)$$

where

$$A_{\text{sym}} = \frac{\partial(\pi_{(\xi_1, \eta_2)} \circ \varphi_0)}{\partial(\xi_2, \eta_1)}, \quad b_{\text{sym}} = \pi_{(\xi_1, \eta_2)}(\Delta\varphi). \quad (19)$$

Numerical evaluation shows that A_{sym} is singular only at $h = h_1$, whereas the orbit at $h = h_2$ remains non-degenerate as a symmetric orbit.

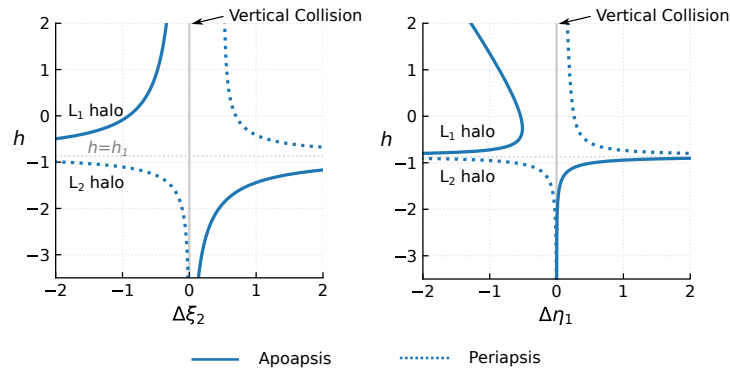


FIGURE 8. Displacements in ξ_2 (left) and η_1 (right) coordinates of the vertical collision orbit of Hill’s problem at apoapsis (q_3 maximal) and periapsis ($q_3 = 0$) under perturbation to halo orbits in the CR3BP.

The solution to the system (18) at the two intersections of the vertical collision orbit with $\xi_3 = 0$ – the apoapsis (q_3 maximal) and periapsis ($q_3 = 0$) – is shown in Figure 8. Since $\Delta\xi_2 \neq 0$, we have $|\xi_0| < 1$ after perturbation, indicating that vertical collision orbits are continued to non-collision orbits. Using the relation $\Delta q_1 = (1 - \xi_0)\Delta\eta_1$, the displacement of the unregularized coordinate q_1 has the same sign as $\Delta\eta_1$. We summarize the observations as follows:

- (1) The vertical collision orbit is degenerate at two energy levels, $h = h_1$ and $h = h_2$. As an r_y -symmetric orbit, the orbit at $h = h_2$ is non-degenerate. Hence, the vertical collision orbit continues for $h \neq h_1$ to an r_y -symmetric orbit after perturbation to the CR3BP by Theorem 2.7.
- (2) For $h < h_1$, the vertical collision orbit continues under perturbation to a symmetric, non-collision L_2 -halo orbit, with apoapsis displaced outward ($q_1 > 1 - \mu$) and periapsis inward ($q_1 < 1 - \mu$) for small μ .
- (3) For $h > h_1$, the vertical collision orbit continues under perturbation to a symmetric, non-collision L_1 -halo orbit, with apoapsis displaced inward ($q_1 < 1 - \mu$) and periapsis outward ($q_1 > 1 - \mu$) for small μ .

4.3. Near-Collision Behavior of Halo Orbits in the Saturn-Enceladus System. As an explicit case of the perturbation from Hill's problem to the CR3BP, we examine the near-collision behavior of halo orbits in the Saturn-Enceladus system ($\mu = 1.901109735892602 \times 10^{-7}$), computed via continuation in the Moser-regularized system.

The bifurcation diagrams of the northern L_1 and L_2 halo families are shown in Figure 9. Compared with Hill's problem, the breaking of the r_x -symmetry in the CR3BP removes the pitchfork bifurcation connecting the vertical collision orbit and the halo families. Consequently, the low-energy branch of the vertical collision orbit connects to the L_2 halo family, while the high-energy branch connects to the L_1 halo family. We refer to the near-vertical continuations of these halo branches as *collisional halo orbits*.

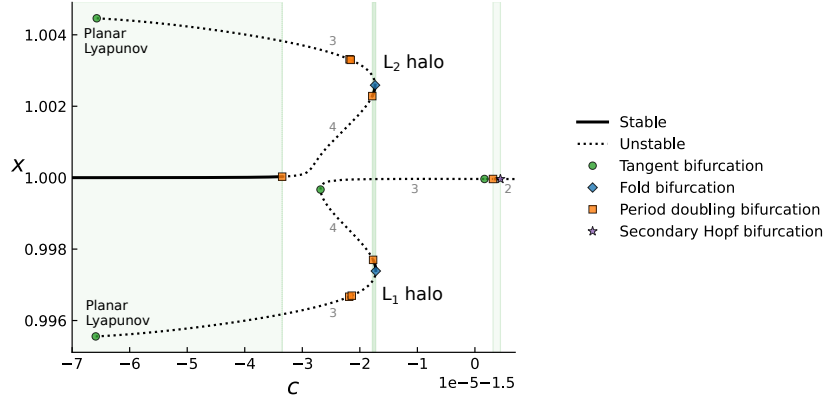


FIGURE 9. Bifurcation diagram of the L_1 and L_2 halo families in the Saturn-Enceladus system. The horizontal axis corresponds to the Jacobi energy $H_\mu = c$, and the vertical axis shows the x -coordinate at the apoapsis.

Figure 10 illustrate the planar-to-collisional transitions of the L_1 and L_2 halo families, respectively. Prior to the collisional branch, the orbits appear in a near symmetric configuration with respect to the plane $x = 1 - \mu$, due to the approximate symmetry r_x continued from the Hill's problem. Beyond the NRHO regime, the orbits become increasingly confined in the yz -plane and acquire a nearly vertical geometry. In this regime, the z -coordinate of the apoapsis grows rapidly for the L_1 family and decreases for the L_2 family, while both retain their vertical structure.

4.4. Bifurcation Surface of Halo Families from $\mu = 0$ to $\mu = 0.5$. To understand the global evolution of the halo families and their relation to the vertical collision orbits, we compute the bifurcation diagrams of the L_1 and L_2 halo orbits for mass ratios $\mu \in [0, 0.5]$ of the rescaled CR3BP Hamiltonian \hat{H}_μ . The Jacobi energy is varied over the range $h \in [-1, 0.4]$ to construct a two-parameter bifurcation surface that continuously connects Hill's problem to the equal-mass case.

The resulting bifurcation surface is shown in Figure 11. For small mass ratios, the L_1 family shows two distinct fold bifurcations, bounding an interval which includes the linearly stable regime

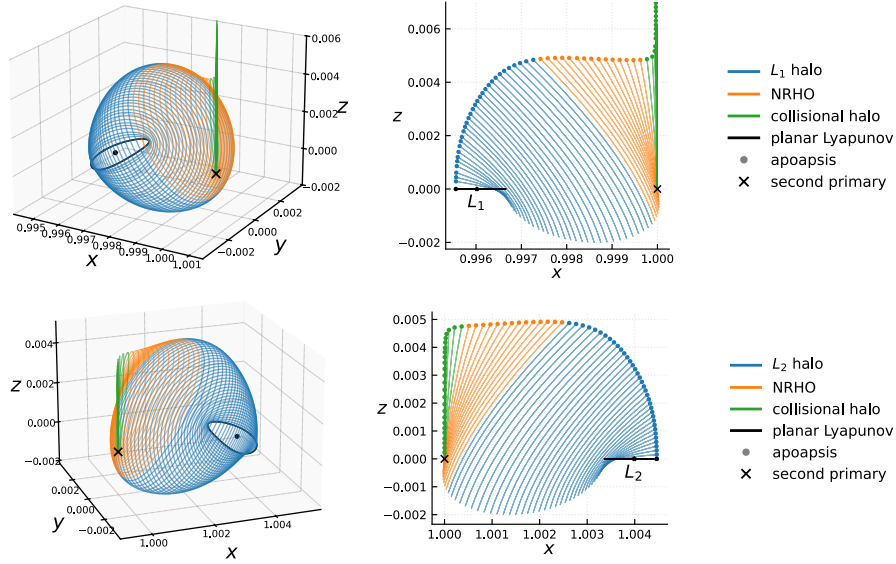


FIGURE 10. Continuation of the L_1 (top) and L_2 (bottom) halo families in the Saturn-Enceladus CR3BP.

corresponding to the *near-rectilinear halo orbits* (NRHOs). A qualitative transition occurs at a critical mass ratio μ^* between $\mu = 0.05$ and $\mu = 0.06$, where the two folds disappear and the Jacobi energy becomes a monotone function along the family. Thus, for most planet-moon systems, the bifurcation structure of the L_1 family includes the same set of degeneracies, with exceptions such as the Pluto-Charon system ($\mu \approx 0.12$). The critical value μ^* corresponds to the upper limit $\mu^* \approx 0.0573$ identified by Howell [How84] for the existence of a linearly stable region of the L_1 halo family. Meanwhile, the third degeneracy at higher energy, corresponding to the pitchfork bifurcation of the vertical collision family described in Section 4.1, persists for $\mu \in [0, 0.5]$.

4.4.1. Earth-Moon Case. The bifurcation diagram of halo orbits in the Earth-Moon system is shown in Figure 12. We observe the same topological structure as in the Saturn-Enceladus system, with the graphs displaying the same sequence of bifurcations but at different parameter scales. The perturbation from Hill’s problem is more pronounced, with less symmetry between L_1 and L_2 halo families and more distorted bifurcation diagrams.

4.4.2. Copenhagen Case ($\mu = 0.5$). We examine the equal-mass case $\mu = 0.5$, known as the *Copenhagen problem*, named after the series of studies carried out at the Copenhagen Observatory under the direction of Strömgren [Str33]. This case possesses additional symmetries: reflection across both the plane $x = 0$ (4) and the y -axis (5) leaves the equations of motion invariant.

The bifurcation diagram for the Copenhagen problem is shown in Figure 13. In contrast to the small- μ regime, the L_1 family no longer goes through fold bifurcations, and its Jacobi energy increases monotonically. The L_2 family retains a fold bifurcation, but the order and position of the period-doubling bifurcations are modified.

Figure 14 shows the L_1 and L_2 halo families of the Copenhagen problem. In this case, the L_1 halo orbits are doubly-symmetric with respect to both reflections r_y across the xz -plane and r_{xz} across the y -axis. The behavior near collision is visibly distinct from the small mass ratio case: the z -coordinate of the apoapsis of the L_1 family increases consistently from the start of the continuation, while for the L_2 family, the orbits contract smoothly toward collision with the second primary.

4.5. W4/W5 families in Hill’s Problem and Earth-Moon System. We study the pair of r_x -symmetric periodic orbits that bifurcate from the second pitchfork bifurcation of the vertical

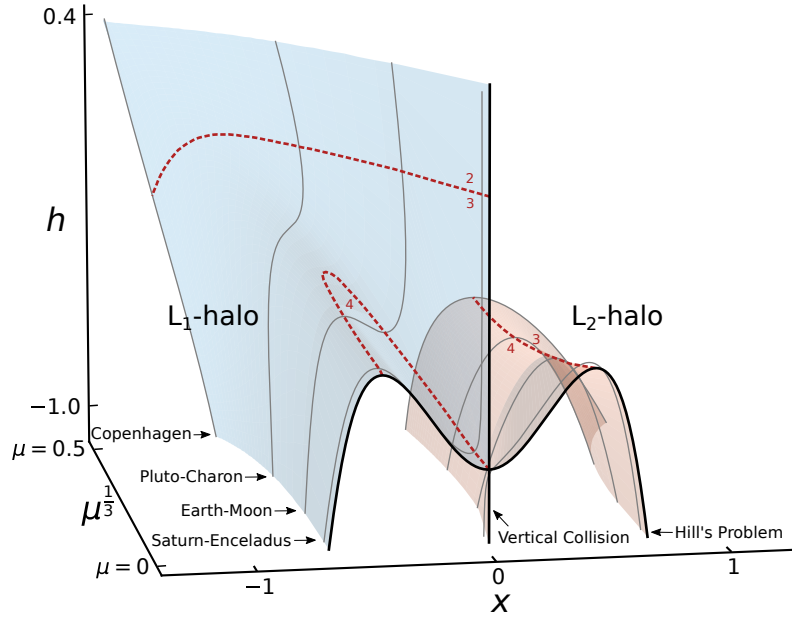


FIGURE 11. Bifurcation surfaces of the L_1 and L_2 halo families for mass ratios $\mu \in [0, 0.5]$ and energy range $h \in [-1.0, 0.4]$. The horizontal axis shows the x -coordinate at the apoapsis. Sections of the surface for selected planet-moon systems, as well as the Hill's problem ($\mu = 0$) and the Copenhagen problem ($\mu = 0.5$), are highlighted. Red dotted curves indicate degeneracies: two associated with fold bifurcations and one with a pitchfork bifurcation at higher energy.

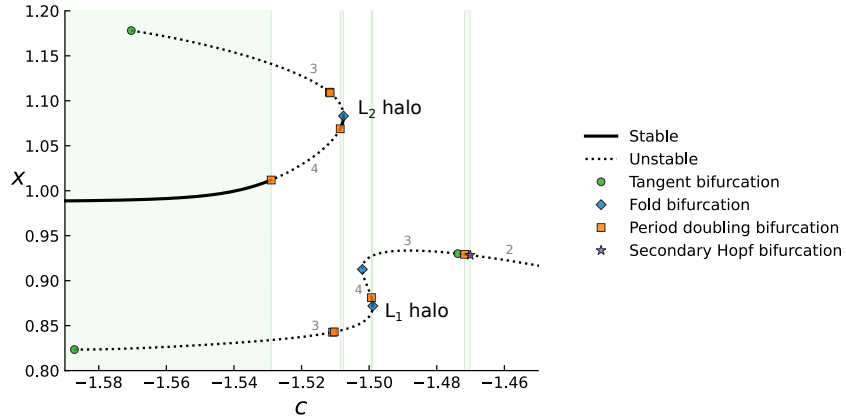


FIGURE 12. Bifurcation diagram of the L_1 and L_2 halo families in the Earth-Moon system. The horizontal axis corresponds to the Jacobi energy $H_\mu = c$, and the vertical axis shows the x -coordinate at the apoapsis.

collision orbit in Hill's problem at energy $h \approx 0.04$, as described in Section 4.1. These orbits correspond after continuation to the Earth-Moon system to the W4/W5 families studied in [Doe+07]. For consistency, we refer to these orbits in the Hill's problem also as the W4/W5 families.

Figure 15 shows the bifurcation graph in Hill's problem. From the pitchfork bifurcation, the two branches emerge in symmetry in the direction of increasing energy. Along each branch, we observe three period-doubling bifurcations: one pair of Floquet multipliers alternates between negative hyperbolic, elliptic, negative hyperbolic again, and finally elliptic, while the other pair

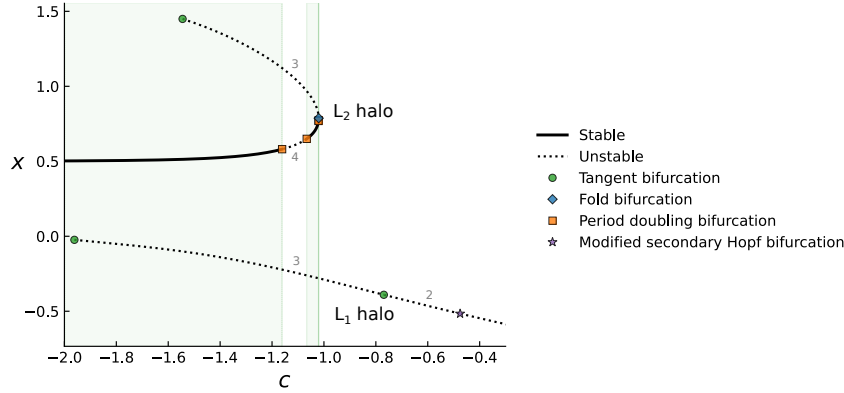


FIGURE 13. Bifurcation diagram of the L_1 and L_2 halo families in the Copenhagen problem ($\mu = 0.5$). The horizontal axis corresponds to the Jacobi energy $H_\mu = c$, and the vertical axis shows the x -coordinate at the apoapsis.

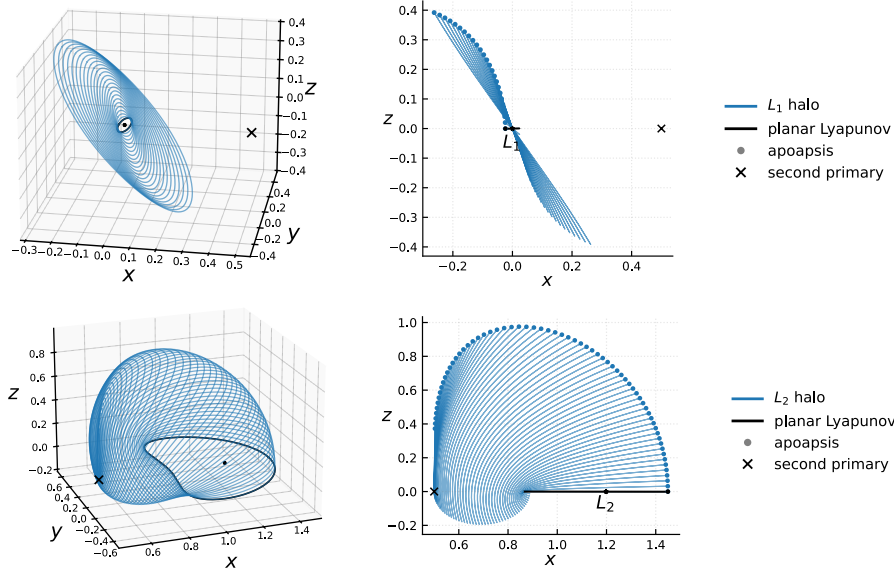


FIGURE 14. Continuation of L_1 (top) and L_2 (bottom) halo orbits in the Copenhagen problem ($\mu = 0.5$).

remains positive hyperbolic. The continuation of the W4 family as it bifurcates from the vertical collision orbit is shown in Figure 16.

As explained in Section 2.5, this pitchfork bifurcation persists under perturbation to the CR3BP because the r_y -symmetry of the pitchfork bifurcation persists. The resulting branches are no longer symmetric orbits in the CR3BP, but instead form two distinct non-symmetric families that connect to the vertical periodic orbits emanating from the equilateral Lagrange points L_4 and L_5 .

Figure 17 shows the corresponding bifurcation graph in the Earth-Moon system, which is continued using the Poincaré section $p_3 = 0$. As in Hill's problem, the two branches bifurcate from the L_1 halo family in the direction of increasing energy and pass through three period-doubling bifurcations. As the energy increases further, the apoapsis y -coordinate starts to decrease until the family connects at energy $c \approx -0.97$ to the vertical periodic orbit associated with L_4 . Figure 18 shows the continuation of the W4 family from the L_1 halo orbit to its termination in the L_4 vertical orbit.

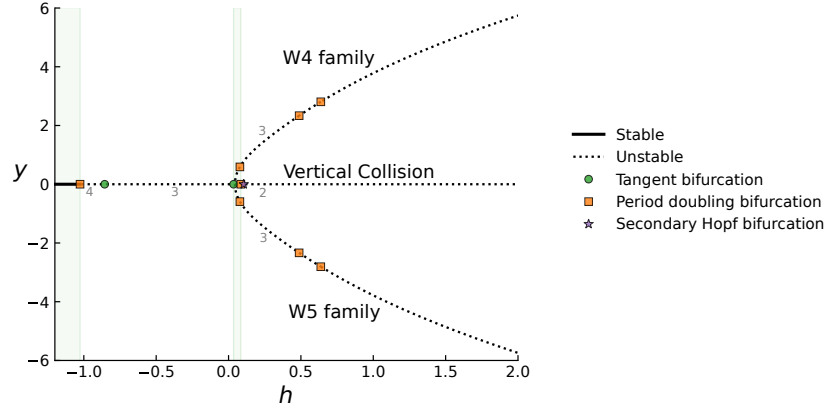


FIGURE 15. Bifurcation diagram of the vertical collision orbit (central line) and the W4 and W5 families of orbits (branches) in Hill's problem. The horizontal axis corresponds to the Hamiltonian energy $\hat{H}_0 = h$, and the vertical axis shows the y -coordinate at the apoapsis.

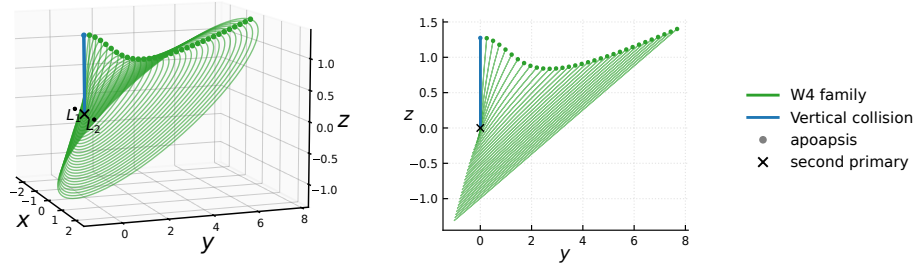


FIGURE 16. Continuation of the W4 family in Hill's problem.

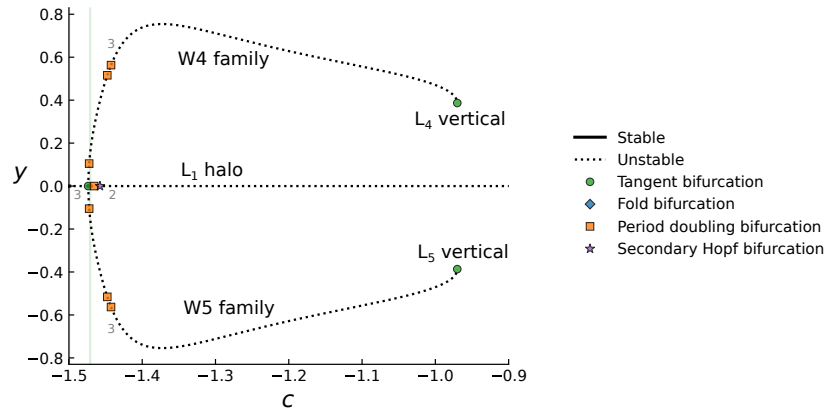


FIGURE 17. Bifurcation diagram of the L_1 halo orbits (central line) and the W4 and W5 families of orbits (branches) in the Earth-Moon system. The horizontal axis corresponds to the Hamiltonian energy $H_\mu = c$, and the vertical axis shows the y -coordinate at the apoapsis.

4.6. Period Doubling Bifurcation and Butterfly Orbit Family. The butterfly orbit family is a well-known class of periodic orbits catalogued in the JPL Periodic Orbit Catalogue [VS18].

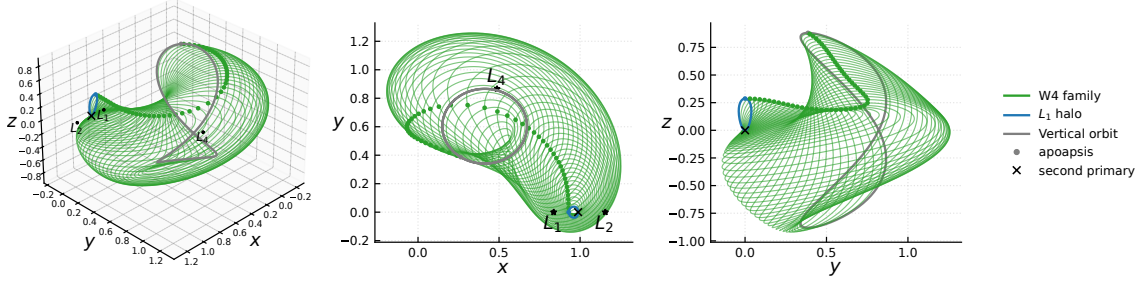


FIGURE 18. Continuation of the W4 family (green) in the Earth-Moon system, from its bifurcation from the L_1 halo orbit (blue) to its termination in the L_4 vertical orbit at L_4 (gray).

These orbits share several characteristics with halo orbits, including a vertical geometry, close proximity to the light primary, and extended coverage of the polar region [Gre+08]. Recently, butterfly orbits in the Saturn-Enceladus system have been proposed as candidate science orbits for a mission to Enceladus due to their coverage of the south polar plume region, which is of high scientific interest because of its active geysers [Boo+24]. In the literature, butterfly orbits have been primarily studied in the Earth-Moon system, where they arise through a period doubling bifurcation of the L_2 halo family [HC99; Whi+18].

By continuation in the Moser regularized rescaled Hamiltonian \hat{H}_μ , we obtain the following characterization of the butterfly orbits:

- (1) In the Hill's problem, the butterfly family arises as a doubly symmetric orbit from a period doubling bifurcation of the vertical collision orbit at energy level $h \approx -1.02$.
- (2) Under perturbation to the CR3BP, the butterfly family emerges as a symmetric orbit from the period doubling bifurcation of the collisional L_2 halo orbit.

Figure 19 shows the bifurcation diagrams of the butterfly family in the Saturn-Enceladus CR3BP and in Hill's problem. In both systems, the butterfly family emerges from a period-doubling bifurcation of either the collisional L_2 -halo or vertical collision family, where the Floquet multipliers change from elliptic-elliptic (stable) to elliptic-negative hyperbolic (unstable). The butterfly branch itself begins with elliptic-positive hyperbolic type and evolves in the direction of decreasing Hamiltonian energy. The family then undergoes a fold bifurcation, after which the energy increases. In both systems, the Floquet multipliers transition to elliptic-elliptic type right after the fold, then immediately transition through a secondary Hopf bifurcation to four complex conjugate multipliers.

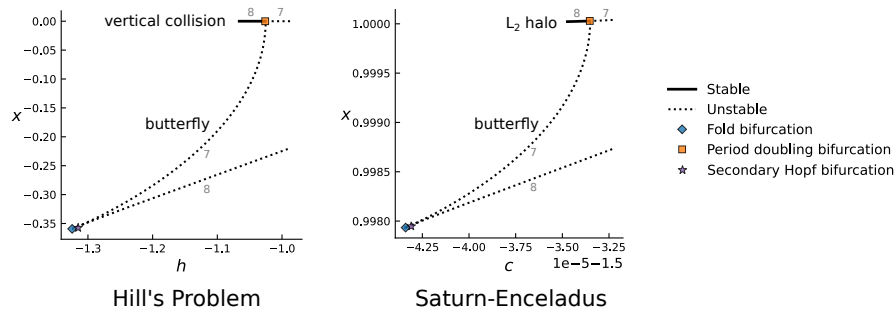


FIGURE 19. Bifurcation diagrams of the butterfly orbit family in the Hill's problem (left) and the Saturn-Enceladus CR3BP (right). The horizontal axis represents the Hamiltonian energy, while the vertical axis shows the x -coordinate at one of the two intersections with the Poincaré section $y = 0$ (specifically, the intersection with the smaller x value).

Figure 20 shows the emergence of the butterfly family in the Saturn-Enceladus system from a period doubling bifurcation of the collisional L_2 halo orbit. At the bifurcation point, the orbit is nearly vertical, with a diameter in the xy -plane of order 10^{-5} length units versus a vertical height of 0.00437 LU (1042 km). The perilune radius is approximately 0.05 km, well below the surface of Enceladus (radius 252.1 km). This is significantly closer to collision than in the Earth-Moon system, where the analogous bifurcation occurs at a perilune radius of about 1830 km [Whi+18]. The emerging butterfly orbit preserves the vertical height of the parent halo orbit while developing two symmetric “wings” extending in the x -direction at apoapsis. After a fold bifurcation, the wings tilt inward and intersect in the xz -projection.

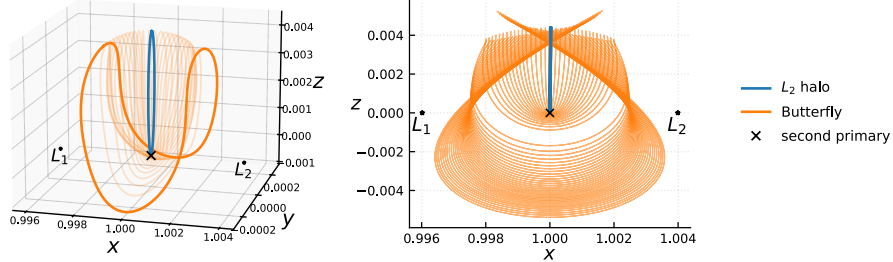


FIGURE 20. Period-doubling bifurcation of the butterfly orbit family from a collisional L_2 halo orbit in the Saturn-Enceladus CR3BP.

4.7. Tri-Fly Orbits from Period Tripling Bifurcations. We examine the period tripling bifurcation of the vertical collision and collisional L_2 halo families, which occurs at an energy level lower than the period doubling bifurcation from which the butterfly family emerges. This period tripling bifurcation gives rise to a set of four periodic orbit families with symmetric configurations. Examples of each of the four orbits are shown in Figure 21. These orbits exhibit a three-lobed structure in the vertical direction and form a triangular pattern in the xy -projection. We refer to these as *tri-fly* orbits to reflect this characteristic geometry. The appearance of these families from the third cover of the vertical collision orbits also appears in [AB25].

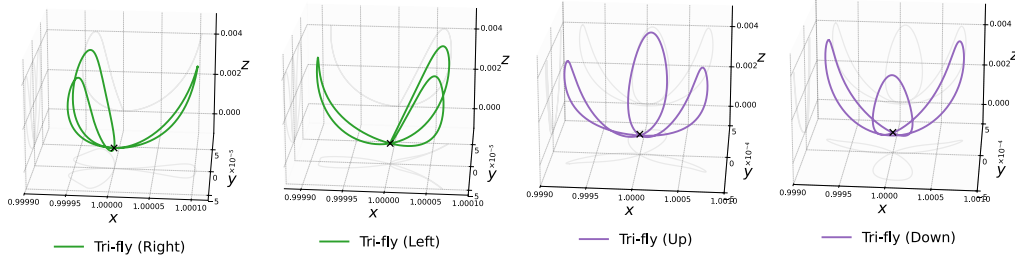


FIGURE 21. Four tri-fly orbits which originate from a period-tripling bifurcation of a collisional L_2 halo orbits in the Saturn-Enceladus system.

The four tri-fly orbits are characterized by the orientation of their triangular structure in the xy -projection: “right”, “left”, “up” and “down”. The “right” and “left” orbits (plotted in green) are symmetric with respect to the reflection r_y , while the “up” and “down” orbits (plotted in purple) are r_x -symmetric in the Hill’s problem but become non-symmetric after perturbation to CR3BP. The “up” and “down” families are exact mirror images of one another with respect to the plane $y = 0$.

Figure 22 shows the bifurcation structure of the tri-fly families in the Hill’s problem and the Saturn-Enceladus systems. In the Hill’s problem, all four tri-fly families emerge simultaneously from the period-tripling bifurcation of the vertical collision orbit. Once we perturb to the CR3BP, the “up” and “down” families do not originate directly from this bifurcation point, but instead

from a separate pitchfork bifurcation along the “left” tri-fly branch. This results in a sequential rather than a simultaneous emergence of the families.

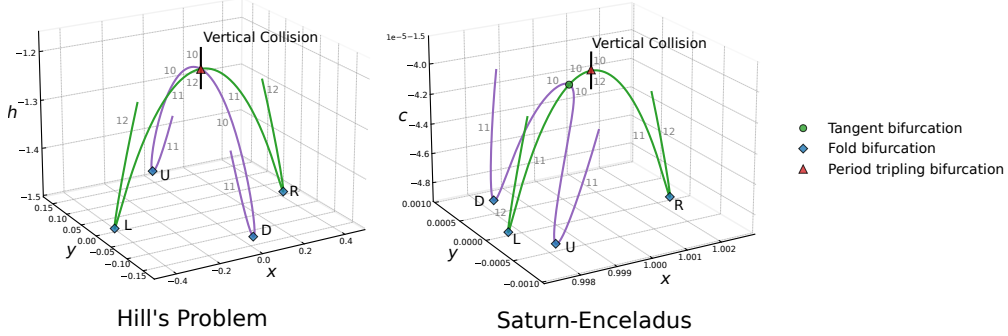


FIGURE 22. Bifurcation graphs of the four tri-fly orbits in the Hill’s problem (left) and the Saturn-Enceladus CR3BP (right). For the “left” and “right” orbits, we plot the coordinates of the point with $p_3 = 0$ on the Poincaré section $y = 0$. For the “up” and “down” orbits in the Hill’s problem, we plot the coordinates of the point with $p_3 = 0$ on the section $x = 0$, which corresponds to the fixed-point locus of the symmetry r_x . For these orbits in the Saturn-Enceladus system, we plot the coordinates of the intersection point with $p_3 = 0$ and $z > 0$, with $y > 0$ for the “up” orbit and $y < 0$ for the “down” orbit.

ACKNOWLEDGEMENTS

Chankyu Joung and Otto van Koert were supported by the National Research Foundation of Korea (NRF), grant number (MSIT) (RS-2023-NR076656), funded by the Korean government. Chankyu Joung was partially supported by BK21 SNU Mathematical Sciences Division. The authors thank Cengiz Aydin for many helpful discussions during the course of this project. Chankyu Joung and Dayung Koh are grateful to Damon Landau at the Jet Propulsion Laboratory for his kind support and for valuable conversations related to Enceladus orbits. Chankyu Joung also thanks Dongho Lee and Beomjun Sohn for their help and assistance throughout the preparation of this work.

APPENDIX A. NUMERICAL IMPLEMENTATION OF RESCALED CR3BP

The rescaled CR3BP Hamiltonian \hat{H}_μ in (6) contains a singular denominator $\mu^{2/3}$. For numerical integration at small μ , we let $\nu = \mu^{1/3}$ and rewrite the Hamiltonian in a convenient form using the identity:

$$\frac{1}{\sqrt{1+x}} - 1 + \frac{x}{2} = x^2 \left(\frac{2 + \sqrt{1+x}}{2\sqrt{1+x}(1 + \sqrt{1+x})^2} \right), \quad x > -1.$$

For $x = 2q_1\nu + |q|^2\nu^2 > -1$, i.e., away from the first primary located at $q = (-\mu^{-\frac{1}{3}}, 0, 0)$, we obtain the numerically convenient form:

$$\hat{H}_\mu(q, p) = \frac{1}{2}|p|^2 - \frac{1}{|q|} + p_1q_2 - p_2q_1 + \frac{1-\mu}{2}|q|^2 - \frac{(1-\mu)(2q_1 + |q|^2\nu)^2(2 + \sqrt{1+2q_1\nu + |q|^2\nu^2})}{2\sqrt{1+2q_1\nu + |q|^2\nu^2}(1 + \sqrt{1+2q_1\nu + |q|^2\nu^2})^2}. \quad (20)$$

This expression is analytic in $\nu = \mu^{1/3}$, and allows accurate numerical evaluation for small μ .

APPENDIX B. RESTRICTED PHASE SPACE

The Moser regularized Hamiltonian described in Section 3.2 fits into the general setting of Hamiltonian systems with constraints [Dir50; Dir67]. Here, we give a brief outline of the method together with a motivating example. We consider a Hamiltonian \tilde{H} on a phase space \mathbb{R}^{2n} with

coordinates (q, p) , which we want to restrict to constraints $f_1(q, p) = \dots = f_{2k}(q, p) = 0$. Let $\omega = \sum_{i=1}^n dp_i \wedge dq_i$ be the standard symplectic form and consider the values

$$A_{ij} = \omega(X_{f_i}, X_{f_j}) = \omega(\nabla f_i, \nabla f_j) = \{f_i, f_j\}, \quad i, j = 1, \dots, 2k \quad (21)$$

where $\{, \}$ denotes the Poisson bracket.

Definition B.1. We call the set $R = \{x \in \mathbb{R}^{2n} \mid f_1(x) = \dots = f_{2k}(x) = 0\}$ the *restricted phase space* if the matrix $[A_{ij}]$ is non-degenerate.

Lemma B.2. *The restricted phase space R is a symplectic submanifold of codimension $2k$ in \mathbb{R}^{2n} .*

Proof. Since $[A_{ij}]$ is non-degenerate, the vector fields X_{f_i} are linearly independent. Hence, R is a regular submanifold of codimension $2k$ in \mathbb{R}^{2n} . Each X_{f_i} is orthogonal to the tangent space of R , since

$$X_{f_i}^T \cdot v = \omega(\nabla f_i, v) = 0, \quad \forall v \in TR.$$

Thus, we have the splitting

$$T\mathbb{R}^{2n}|_R = \langle X_{f_1}, \dots, X_{f_{2k}} \rangle \oplus TR.$$

With respect to this splitting, the matrix representation of ω is block diagonal:

$$[\omega] = \begin{pmatrix} [A_{ij}] & 0 \\ 0 & [\omega]|_{TR} \end{pmatrix}.$$

The upper-left block is non-degenerate by assumption, and since ω is non-degenerate, the lower-right block must also be non-degenerate. Hence R is a symplectic submanifold. \square

Our goal is to study the dynamics on R given by the restricted Hamiltonian $H := \tilde{H}|_R$.

Lemma B.3. *The Hamiltonian vector field on the restricted phase space is given by*

$$X_H = X_{\tilde{H}} + \sum_{i=1}^{2k} c_i X_{f_i}$$

where $c_i = \sum_{j=1}^{2k} (A^{-1})_{ij} \{\tilde{H}, f_j\}$ and A is the matrix defined in (21).

Proof. By the definition of Hamiltonian vector fields,

$$i_{X_H} \omega = -d(H|_R) = -(dH)|_{TR} = (i_{X_{\tilde{H}}} \omega)|_{TR}.$$

Hence, the projection of $X_{\tilde{H}}$ to TR agrees with X_H on R . We write

$$X_{\tilde{H}} = X_H + \sum_{i=1}^{2k} c_i X_{f_i}.$$

Taking the symplectic inner product with X_{f_j} gives

$$\omega(X_{\tilde{H}}, X_j) = \sum_{i=1}^{2k} c_i \omega(X_{f_i}, X_{f_j}), \quad j = 1, \dots, 2k.$$

Solving this linear system for c_i gives the stated formula. \square

Example B.4 (Mathematical Pendulum). We start with the unconstrained Hamiltonian of a particle in linear potential. In polar coordinates, such a Hamiltonian reads

$$H_0 = \frac{1}{2} \left(p_r^2 + \frac{p_\varphi^2}{r^2} \right) - gr \cos \varphi.$$

The unconstrained Hamiltonian equations are given by

$$(\dot{r}, \dot{\varphi}, \dot{p}_r, \dot{p}_\varphi) = \left(p_r, \frac{p_\varphi}{r^2}, \frac{p_\varphi^2}{r^3} + g \cos \varphi, -gr \sin \varphi \right).$$

The constraints are given by $f_1 = r - 1$ and $f_2 = p_r$. The Poisson brackets are then

$$\{f_1, f_2\} = 1, \quad \{f_1, H\} = p_r, \quad \{f_2, H\} = \frac{p_\varphi^2}{r^3} + g \cos \varphi$$

Together with the Hamiltonian vector fields X_{f_1} and X_{f_2} , we get the Hamiltonian vector field on the restricted phase space. This is

$$(\dot{r}, \dot{\varphi}, \dot{p}_r, \dot{p}_\varphi) = (0, \frac{p_\varphi}{r^2}, 0, -gr \sin \varphi),$$

which are the equations for the mathematical pendulum.

APPENDIX C. DETAILS OF DIFFERENTIAL CORRECTION IN MOSER REGULARIZATION

We derive the Jacobian matrix used in the differential correction scheme formulated in Moser regularized coordinates (Section 3.4). We consider a Moser regularized Hamiltonian Q corresponding to the original Hamiltonian H , and apply corrections for a fixed energy level $H = c$. The procedure described here is valid for general (non-symmetric) periodic orbits; for symmetric cases, the reduced formulation in Section 3.4 can be applied analogously.

We work with the Poincaré section $\xi_3 = 0$ and define the vector of free variables as

$$X = (\xi_1, \xi_2, \eta_1, \eta_2, \tau),$$

where τ denotes the (predicted) period of the orbit. The remaining variables ξ_0 , η_0 , and η_3 are determined from the three constraint equations:

$$f_1 = |\xi|^2 - 1 = 0, \quad f_2 = \xi \cdot \eta = 0, \quad Q(\xi, \eta) = \frac{1}{2g}.$$

From the first two constraints we obtain

$$\xi_0 = \sqrt{1 - \xi_1^2 - \xi_2^2}, \quad \eta_0 = \frac{1}{\xi_0}(\xi_1\eta_1 + \xi_2\eta_2),$$

and η_3 is determined by numerically solving the energy constraint $Q(\xi, \eta) = 1/(2g)$ near a predicted value, for instance using Brent's method [Bre71].

Periodic orbits satisfy the constraint function

$$F(X) = p \circ \varphi^\tau(\xi_0, \xi_1, \xi_2, 0; \eta_0, \eta_1, \eta_2, \eta_3) - (\xi_1, \xi_2, 0, \eta_1, \eta_2),$$

where φ^τ denotes the flow of the Hamiltonian vector field X_Q for time τ , and p is the projection onto $(\xi_1, \xi_2, \xi_3, \eta_1, \eta_2)$. The correction proceeds via Newton iterations:

$$X_{i+1} = X_i - DF(X_i)^{-1}F(X_i), \quad i = 0, 1, 2, \dots,$$

until convergence, i.e., when $|F(X_i)| < 10^{-10}$.

To compute the Jacobian DF , we first evaluate the derivatives of the dependent variables with respect to the free variables. The expressions are:

$$\begin{aligned} \frac{\partial \xi_0}{\partial \xi_i} &= -\frac{\xi_i}{\sqrt{1 - \xi_1^2 - \xi_2^2}}, \quad i = 1, 2, \\ \frac{\partial \eta_0}{\partial \xi_0} &= -\frac{\xi_1\eta_1 + \xi_2\eta_2}{\xi_0^2}, \quad \frac{\partial \eta_0}{\partial \xi_i} = -\frac{\eta_i}{\xi_0}, \quad \frac{\partial \eta_0}{\partial \eta_i} = -\frac{\xi_i}{\xi_0}, \quad i = 1, 2, \\ \frac{\partial \eta_3}{\partial \xi_i} &= \left(\frac{\partial Q}{\partial \eta_3}\right)^{-1} \frac{\partial Q}{\partial \xi_i}, \quad \frac{\partial \eta_3}{\partial \eta_i} = \left(\frac{\partial Q}{\partial \eta_3}\right)^{-1} \frac{\partial Q}{\partial \eta_i}, \quad i = 0, 1, 2. \end{aligned}$$

The columns of the Jacobian matrix DF can be computed from these derivatives together with the linearized flow $d\varphi^\tau$, which we obtain by integrating the first-order variational equations along the trajectory. For example, the derivative with respect to ξ_1 is given by

$$\frac{\partial F}{\partial \xi_1} = dp \circ d\varphi^\tau \circ \begin{bmatrix} \frac{\partial \xi_0}{\partial \xi_1} & 1 & 0 & 0 & 0 & \frac{\partial \eta_0}{\partial \xi_1} & 0 & \frac{\partial \eta_3}{\partial \xi_1} \end{bmatrix}^T - [1 \ 0 \ 0 \ 0 \ 0]^T,$$

and similarly for the variables ξ_2 , η_1 , η_2 . The derivative with respect to the time variable τ is

$$\frac{\partial F}{\partial \tau} = dp \circ X_Q(\varphi^\tau(\xi_0, \xi_1, \xi_2, 0; \eta_0, \eta_1, \eta_2, \eta_3)).$$

APPENDIX D. BIFURCATION ANALYSIS VIA CONLEY-ZEHNDER INDICES

To a non-degenerate periodic Hamiltonian orbit γ one can associate an integer valued invariant $\mu_{CZ}(\gamma)$ called the *Conley-Zehnder index* [CZ84]. Intuitively, this invariant measures the winding number of the linearized flow along γ . We recall two important properties most relevant for our purposes:

- (1) (invariance along non-degenerate families) Let γ_s be a continuous family of non-degenerate periodic orbits of Hamiltonians H_s . Then the Conley-Zehnder index is constant along the family:

$$\mu_{CZ}(\gamma_s) = \mu_{CZ}(\gamma_{s_0}) \quad \text{for all } s.$$

- (2) (index jump implies bifurcation) Let γ_s be a continuous family of isolated periodic orbits of Hamiltonians H_s . If $\gamma_{s_0 \pm \varepsilon}$ are non-degenerate and satisfy

$$\mu_{CZ}(\gamma_{s_0 - \varepsilon}) \neq \mu_{CZ}(\gamma_{s_0 + \varepsilon}),$$

then there is a bifurcation occurring in the interval $(s_0 - \varepsilon, s_0 + \varepsilon)$ generating at least one additional orbit. This follows from the behavior of local Floer homology; see Section 3.2 of [Gin10].

These properties make the Conley-Zehnder index an effective tool for classification of periodic orbit families and bifurcation analysis. For instance, it has been used in recent bifurcation studies of periodic orbits in the CR3BP and related systems [Mor+24; AB25; JvK25; Lee25; Ayd25].

Here we recall a precise definition of the Conley-Zehnder index following the paper of Salamon and Zehnder [SZ92]. First, we consider a path $\psi : [0, 1] \rightarrow Sp(2n)$ of symplectic matrices which is non-degenerate, meaning $\psi(1)$ has no eigenvalue equal to 1. Extend ψ to a path $\tilde{\psi} : [0, 2] \rightarrow Sp(2n)$ ending at either $W_+ = -\text{id}$ or $W_- = \text{diag}(2, 1/2, -1, \dots, -1)$ in such a way that the extension avoids intersecting with the Maslov cycle

$$V = \{\psi \in Sp(2n) \mid \det(\psi - \text{id}) = 0\}.$$

Definition D.1. The **Conley-Zehnder index** of a non-degenerate path $\psi : [0, 1] \rightarrow Sp(2n)$ is defined by

$$\mu_{CZ}(\psi) = \deg \left(\rho(\tilde{\psi})^2 \right),$$

where $\rho(A) = (AA^T)^{-1/2}A \in U(n)$ for $A \in Sp(2n)$.

In other words, the extended path $\tilde{\psi}$ retracts to a *loop* of unitary matrices based at the identity after taking the square, and the Conley-Zehnder index measures the winding number of the loop in the circle obtained by taking the complex determinant.

For a periodic Hamiltonian orbit γ , the Conley-Zehnder index $\mu_{CZ}(\gamma)$ is defined as the index of the symplectic path representing the transverse linearized flow along γ . This requires choosing a suitable symplectic frame along the orbit. In this work, we follow the computation methods, including the choice of frames and extension procedures, described in [Mor+24]. For vertical collision orbits, we take as transverse frame $\{\partial_{\xi_1}, \partial_{\xi_2}, \partial_{\eta_1}, \partial_{\eta_2}\}$. By Property 1, the index is constant along any non-degenerate family of periodic orbits, so it suffices to compute the index at a single orbit in the family.

The resulting Conley-Zehnder indices are shown as labels in the bifurcation graphs in Figures 5, 9, 11, 12, 13, 15, 17, 19, 22 and summarized in Table 1.

REFERENCES

- [AB25] Cengiz Aydin and Alexander Batkhin. “Studying network of symmetric periodic orbit families of the Hill problem via symplectic invariants”. In: *Celestial Mech. Dynam. Astronom.* 137.2 (2025), Paper No. 12, 77.
- [Ayd25] Cengiz Aydin. “Exploration of vertical self-resonant bifurcations from DRO in the Earth-Moon CR3BP”. In: *arXiv preprint arXiv:2508.17286* (2025).
- [BB09] AB Batkhin and NV Batkhina. “Hierarchy of periodic solutions families of spatial Hill’s problem”. In: *Solar System Research* 43.2 (2009), pp. 178–183.

- [BB79] John V Breakwell and John V Brown. “The ‘halo’ family of 3-dimensional periodic orbits in the Earth-Moon restricted 3-body problem”. In: *Celestial mechanics* 20.4 (1979), pp. 389–404.
- [BFvK19] Edward Belbruno, Urs Frauenfelder, and Otto van Koert. “A family of periodic orbits in the three-dimensional lunar problem”. In: *Celestial Mech. Dynam. Astronom.* 131.2 (2019), Paper No. 7, 22.
- [BI21] Francesco Biscani and Dario Izzo. “Revisiting high-order Taylor methods for astrodynamics and celestial mechanics”. In: *Monthly Notices of the Royal Astronomical Society* 504.2 (2021), pp. 2614–2628.
- [Boo+24] Spencer Boone, Andrea Bellome, Joan Pau Sánchez Cuartielles, and Stéphanie Lizy-Destrez. “Approach strategies for inserting into Enceladus science orbit configurations”. In: *75th International Astronautical Congress (IAC)*. 2024.
- [Bre71] R. P. Brent. “An algorithm with guaranteed convergence for finding a zero of a function”. In: *Comput. J.* 14 (1971), pp. 422–425.
- [BV07] A. D. Bruno and V. P. Varin. “Periodic solutions of the restricted three-body problem for a small mass ratio”. In: *Prikl. Mat. Mekh.* 71.6 (2007), pp. 1034–1066.
- [Cam99] Eric Thomas Campbell. “Bifurcations from families of periodic solutions in the circular restricted problem with application to trajectory design”. PhD thesis. Purdue University, 1999.
- [CFvK17] Kai Cieliebak, Urs Frauenfelder, and Otto van Koert. “Periodic orbits in the restricted three-body problem and Arnold’s J^+ -invariant”. In: *Regul. Chaotic Dyn.* 22.4 (2017), pp. 408–434.
- [CZ84] Charles Conley and Eduard Zehnder. “Morse-type index theory for flows and periodic solutions for Hamiltonian equations”. In: *Comm. Pure Appl. Math.* 37.2 (1984), pp. 207–253.
- [Dir50] P. A. M. Dirac. “Generalized Hamiltonian dynamics”. In: *Canad. J. Math.* 2 (1950), pp. 129–148.
- [Dir67] Paul A. M. Dirac. *Lectures on quantum mechanics*. Vol. 2. Belfer Graduate School of Science Monographs Series. Second printing of the 1964 original. Belfer Graduate School of Science, New York; produced and distributed by Academic Press, Inc., New York, 1967, pp. v+87.
- [Doe+07] E. J. Doedel, V. A. Romanov, R. C. Paffenroth, H. B. Keller, D. J. Dichmann, J. Galán-Vioque, and A. Vanderbauwhede. “Elemental periodic orbits associated with the libration points in the circular restricted 3-body problem”. In: *Internat. J. Bifur. Chaos Appl. Sci. Engrg.* 17.8 (2007), pp. 2625–2677.
- [FvK18] Urs Frauenfelder and Otto van Koert. *The restricted three-body problem and holomorphic curves*. Pathways in Mathematics. Birkhäuser/Springer, Cham, 2018, pp. xi+374.
- [Gin10] Viktor L. Ginzburg. “The Conley conjecture”. In: *Ann. of Math. (2)* 172.2 (2010), pp. 1127–1180.
- [Góm+01] G. Gómez, J. Llibre, R. Martínez, and C. Simó. *Dynamics and mission design near libration points. Vol. I*. Vol. 2. World Scientific Monograph Series in Mathematics. Fundamentals: the case of collinear libration points, With a foreword by Walter Flury. World Scientific Publishing Co., Inc., River Edge, NJ, 2001, pp. xviii+443.
- [Gre+08] Daniel J Grebow, Martin T Ozimek, Kathleen C Howell, and David C Folta. “Multi-body orbit architectures for lunar south pole coverage”. In: *Journal of Spacecraft and Rockets* 45.2 (2008), pp. 344–358.
- [HB84] K. C. Howell and J. V. Breakwell. “Almost rectilinear halo orbits”. In: *Celestial Mech.* 32.1 (1984), pp. 29–52.
- [HC99] K. C. Howell and E. T. Campbell. “Three-dimensional periodic solutions that bifurcate from halo families in the circular restricted three-body problem”. In: *Advances in the astronautical sciences* 102 (1999), pp. 891–910.
- [Hén97] Michel Hénon. *Generating families in the restricted three-body problem*. Vol. 52. Lecture Notes in Physics. New Series m: Monographs. Springer-Verlag, Berlin, 1997, pp. xii+278.

- [Hil78] G. W. Hill. “Researches in the Lunar Theory”. In: *Amer. J. Math.* 1.3 (1878), pp. 245–260.
- [HM87] J. E. Howard and R. S. MacKay. “Linear stability of symplectic maps”. In: *J. Math. Phys.* 28.5 (1987), pp. 1036–1051.
- [How84] Kathleen Connor Howell. “Three-dimensional, periodic, “halo” orbits”. In: *Celestial Mech.* 32.1 (1984), pp. 53–71.
- [JvK25] Chankyu Joung and Otto van Koert. “Computational symplectic topology and symmetric orbits in the restricted three-body problem”. In: *Nonlinearity* 38.2 (2025), Paper No. 025015, 27.
- [KS65] P. Kustaanheimo and E. Stiefel. “Perturbation theory of Kepler motion based on spinor regularization”. In: *J. Reine Angew. Math.* 218 (1965), pp. 204–219.
- [Kuz23] Yuri A. Kuznetsov. *Elements of applied bifurcation theory*. Fourth. Vol. 112. Applied Mathematical Sciences. Springer, Cham, 2023, pp. xxvi+703.
- [Lee25] Dongho Lee. “Conley-Zehnder Indices of Spatial Rotating Kepler Problem”. In: *arXiv preprint arXiv:2506.14325* (2025).
- [LL83] ML Lidov and VA Liakhova. “Families of spatial periodic orbits of Hill’s problem and their stability.” In: *Kosmicheskie Issledovaniia* 21 (1983), pp. 3–11.
- [Mac+21] Shannon M MacKenzie, Marc Neveu, Alfonso F Davila, Jonathan I Lunine, Kathleen L Craft, Morgan L Cable, Charity M Phillips-Lander, Jason D Hofgartner, Jennifer L Eigenbrode, J Hunter Waite, et al. “The Enceladus Orbilander mission concept: Balancing return and resources in the search for life”. In: *The Planetary Science Journal* 2.2 (2021), p. 77.
- [MHO09] Kenneth R. Meyer, Glen R. Hall, and Dan Offin. *Introduction to Hamiltonian dynamical systems and the N-body problem*. Second. Vol. 90. Applied Mathematical Sciences. Springer, New York, 2009, pp. xiv+399.
- [Mor+24] Agustin Moreno, Cengiz Aydin, Otto van Koert, Urs Frauenfelder, and Dayung Koh. “Bifurcation Graphs for the CR3BP via Symplectic Methods: On the Jupiter-Europa and Saturn-Enceladus Systems”. In: *The Journal of the Astronautical Sciences* 71 (2024).
- [Mos70] J. Moser. “Regularization of Kepler’s problem and the averaging method on a manifold”. In: *Comm. Pure Appl. Math.* 23 (1970), pp. 609–636.
- [MS82] Kenneth R. Meyer and Dieter S. Schmidt. “Hill’s lunar equations and the three-body problem”. In: *J. Differential Equations* 44.2 (1982), pp. 263–272.
- [MSS05] Juan J. Morales-Ruiz, Carles Simó, and Sergi Simon. “Algebraic proof of the non-integrability of Hill’s problem”. In: *Ergodic Theory Dynam. Systems* 25.4 (2005), pp. 1237–1256.
- [MZ05] Jürgen Moser and Eduard J. Zehnder. *Notes on dynamical systems*. Vol. 12. Courant Lecture Notes in Mathematics. New York University, Courant Institute of Mathematical Sciences, New York; American Mathematical Society, Providence, RI, 2005, pp. viii+256.
- [NAS] NASA. *Gateway - NASA*. Accessed: 2025-11-14. URL: <https://www.nasa.gov/mission/gateway/>.
- [Per83] L. M. Perko. “Periodic solutions of the restricted problem that are analytic continuations of periodic solutions of Hill’s problem for small $\mu > 0$ ”. In: *Celestial Mech.* 30.2 (1983), pp. 115–132.
- [RL09] Ryan P Russell and Martin Lara. “On the design of an Enceladus science orbit”. In: *Acta Astronautica* 65.1-2 (2009), pp. 27–39.
- [SS00] C. Simó and T. J. Stuchi. “Central stable/unstable manifolds and the destruction of KAM tori in the planar Hill problem”. In: *Phys. D* 140.1-2 (2000), pp. 1–32.
- [Str33] Elis Strömberg. “Connaissance actuelle des orbites dans le problème des trois corps”. In: *Bulletin Astronomique, vol. 9, pp. 87-130* 9 (1933), pp. 87–130.
- [SZ92] Dietmar Salamon and Eduard Zehnder. “Morse theory for periodic solutions of Hamiltonian systems and the Maslov index”. In: *Comm. Pure Appl. Math.* 45.10 (1992), pp. 1303–1360.

- [VS18] Mar Vaquero and Juan Senent. “Poincaré: A multi-body, multi-system trajectory design tool”. In: *7th International Conference on Astrodynamics Tools and Techniques*. 2018, pp. 1–12.
- [Whi+18] Ryan J Whitley, Diane C Davis, Laura M Burke, Brian P McCarthy, Rolfe J Power, Melissa L McGuire, and Kathleen C Howell. “Earth-Moon near rectilinear halo and butterfly orbits for lunar surface exploration”. In: *AAS/AIAA Astrodynamics Specialists Conference, Snowbird, Utah*. 2018.
- [ZHD20] Emily M. Zimovan-Spreen, Kathleen C. Howell, and Diane C. Davis. “Near rectilinear halo orbits and nearby higher-period dynamical structures: orbital stability and resonance properties”. In: *Celestial Mech. Dynam. Astronom.* 132.5 (2020), Paper No. 28, 25.